frontiers | Frontiers in Earth Science

Spatial- and temporal-interpolations for efficient hybrid wave numerical simulations

Hao Shen[1,2], Xiaotian Tang[1,2], Chao Lyu[1,3]* and Liang Zhao[1,2]

[1]State Key Laboratory of Lithospheric Evolution, Institute of Geology and Geophysics, Chinese Academy of Sciences, Beijing, China, [2]College of Earth and Planetary Sciences, University of Chinese Academy of Science, Beijing, China, [3]Department of Earth and Planetary Science, University of California, Berkeley, Berkeley, CA, United States

The hybrid simulation method is developed for simulating wave propagation only in a localized heterogeneous media with hybrid inputs obtained once for all from a known reference model. Despite the fact that the hybrid simulation method has a wide range of applications in computational seismology, the associated error control of this method has received relatively little attention in previous research works. We quantitatively discuss the error of the two-step hybrid method in acoustic wave cases and propose a spatial refinement scheme to compute hybrid inputs based on the multi-elements spline interpolation, which is preferable to traditional Lagrange interpolation since it uses more polydirectional interpolated points. This method can also be used for local refinement of wavefield in more general applications, such as saving smooth wavefield in the full-waveform inversion framework. Furthermore, to save memory requirements, hybrid inputs are proposed to be sparsely stored with a high upsampling ratio during the global simulation, and the Fourier interpolation method is introduced to recover them to their original time series. To demonstrate the effect of the proposed methods, we perform several 2D and 3D hybrid wave numerical simulations using the spectral element method. We find that when the global and local meshing differs, the proposed spatial interpolation method can appreciably reduce the error of the hybrid waveforms caused by inaccurate hybrid inputs. We also point out that the Fourier interpolation can efficiently recover the original waveform, allowing hybrid inputs to be stored with time steps toward the Nyquist limit. Our method is expected to become a standard method to reduce the error of hybrid waveforms and save the memory requirements during hybrid simulations and has potential implications for further improving the accuracy of the so-called box tomography.

KEYWORDS

wave propagation, hybrid simulation, full-wave inversion, acoustic wave, Fourier, interpolation, spectral element method (SEM)

1 Introduction

High-resolution seismic images of Earth's structure play a key role in improving our understanding of the dynamic evolution mechanism and material cycling process of the Earth's interior (Replumaz et al., 2004; Zhao et al., 2012; Van Der Meer et al., 2014). In recent years, with the development of computer technology and numerical simulation method, full-waveform inversion (FWI) (Tarantola, 1984; Virieux and Operto, 2009; Fichtner, 2010; Capdeville and Métivier, 2018; Tromp, 2020; Lyu et al., 2021) has emerged as a significant imaging technique. In contrast to ray tomography, FWI uses more information about the waveform (e.g., body and surface waves) to capture the full physics of seismic wave propagation through numerical simulation methods such as the finite-difference method (FDM) (Kelly et al., 1976; Robertsson et al., 1994) and spectral element method (SEM) (Seriani and Priolo, 1994; Komatitsch and Tromp, 1999; Komatitsch et al., 2000; Lyu et al., 2020), and the Earth model is iteratively updated using the adjoint technique (Tarantola, 1988; Tromp et al., 2005) until a convergent fit between synthetic seismograms and observations is achieved. In the past decades, there has been an increasing number of adjoint tomography models at the regional (Tape et al., 2009; Zhu et al., 2012; Chen et al., 2017) and global scales (French and Romanowicz, 2015; Bozdağ et al., 2016; Lei et al., 2020). However, producing detailed structures of interest in the global tomography model or utilizing the information from remote sources and stations in regional inversion requires too many computing resources. Because it is necessary to recalculate the synthetic waveforms, at each iteration, in the global domain, including the sources and receivers, while the model is only updated in a small region. This leads to significant computational costs, especially when shorter periods are included. The so-called "box tomography" (Masson and Romanowicz, 2017a) that relies on the hybrid simulation method can effectively overcome this problem because almost all the forward and backward numerical simulations of wave propagation are confined to the smallest computational domain. Clouzet et al. (2018) applied this method to image the upper-mantle shear velocity and radial anisotropy structures beneath the North American continent. In their study, based on the 3D reference model SEMUCB (French and Romanowicz, 2015), besides data from 155 events with sources located within the study region, the data set includes data (down to 40s) from 122 remote events with sources located outside of the study region, which allows better azimuthal coverage of the study region than the traditional regional dataset with all the events inside the box. Similarly, Wang et al. (2016) image the 3D velocity structures beneath the western Pyrenees revealed by teleseismic P waves using the SEM-DSM hybrid method (Monteiller et al., 2015) in a higher frequency (down to 5s) for the 1D background model.

Hybrid simulation methods can be classified into real-time methods (Capdeville et al., 2003) and two-step methods (Wen
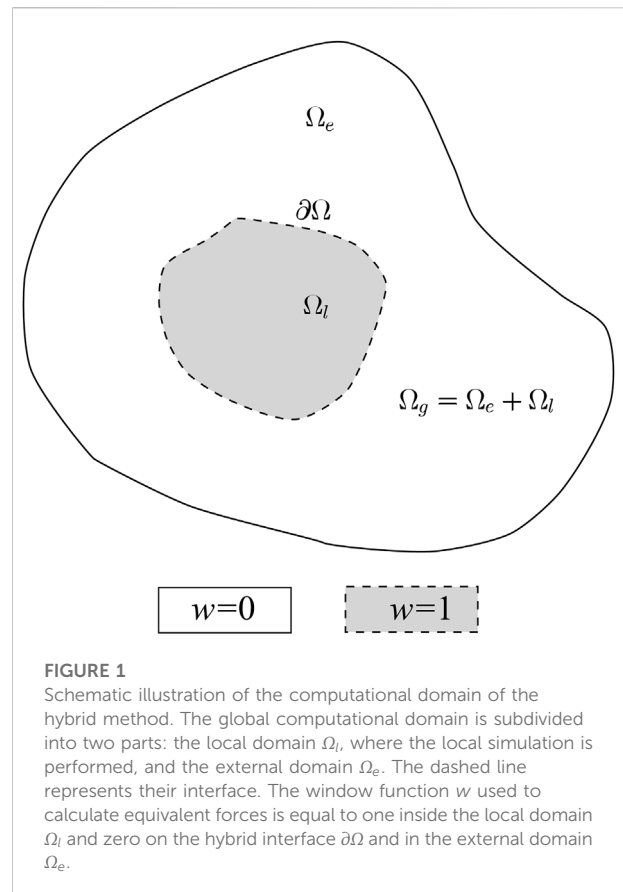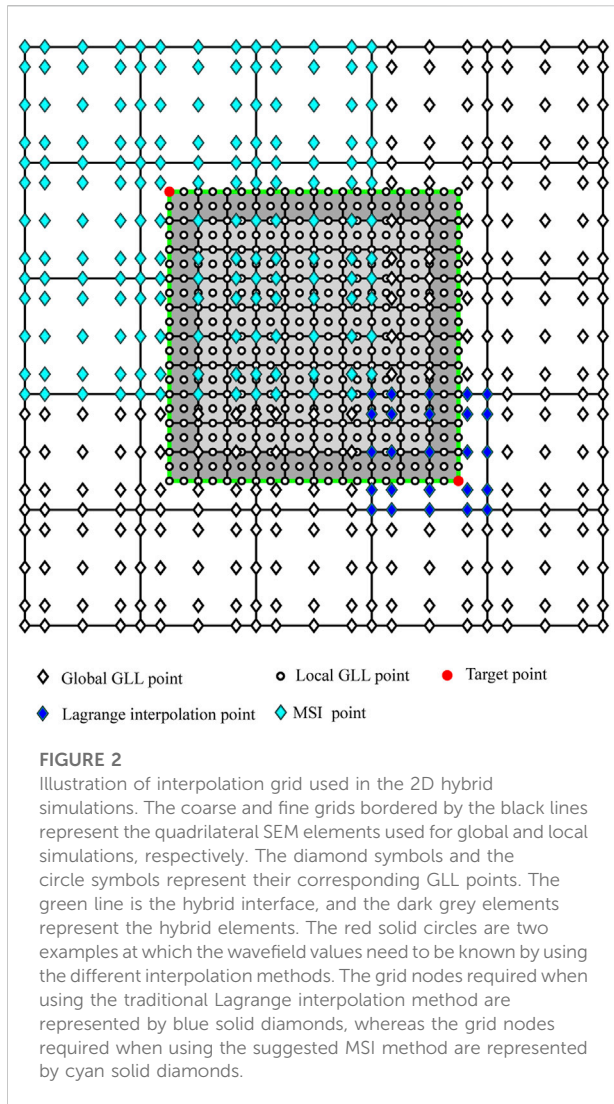

FIGURE 1
Schematic illustration of the computational domain of the hybrid method. The global computational domain is subdivided into two parts: the local domain Ω_l, where the local simulation is performed, and the external domain Ω_e. The dashed line represents their interface. The window function w used to calculate equivalent forces is equal to one inside the local domain Ω_l and zero on the hybrid interface $\partial\Omega$ and in the external domain Ω_e.

and Helmberger, 1998; Robertsson and Chapman, 2000; Wen, 2002; Bielak et al., 2003; Zhao et al., 2008; Masson et al., 2014). In this study, we only focus on the two-step method. The computational domain of the hybrid method is often subdivided into two parts in which wave propagation is simulated separately (Figure 1). The main advantage of the two-step method, also known as the domain reduction method (Bielak et al., 2003; Yoshimura et al., 2003), is that the computation can be limited to a subregion containing the local structural perturbations, avoiding repeated expensive simulations in the global model. First, wave propagation is simulated in a global reference model, and the hybrid inputs (including different physical quantities used to construct the equivalent forces, see below for detailed benchmark of different hybrid methods, and the physical quantities used in this study are illustrated in Section 2.3) are synchronously computed and stored versus time. Then, the equivalent forces are imposed onto the hybrid interface of the local target volume to perform the local simulation. The core of the two-step method is the calculation of the hybrid inputs. This divides into the physical, numerical, and combined three different categories, the multiple point sources method, where the surface integral(s) of the representation theorem are physically discretized to express the hybrid inputs containing the physical

FIGURE 2
Illustration of interpolation grid used in the 2D hybrid
simulations. The coarse and fine grids bordered by the black lines
represent the quadrilateral SEM elements used for global and local
simulations, respectively. The diamond symbols and the
circle symbols represent their corresponding GLL points. The
green line is the hybrid interface, and the dark grey elements
represent the hybrid elements. The red solid circles are two
examples at which the wavefield values need to be known by using
the different interpolation methods. The grid nodes required when
using the traditional Lagrange interpolation method are
represented by blue solid diamonds, whereas the grid nodes
required when using the suggested MSI method are represented
by cyan solid diamonds.

traction and/or displacement (Monteiller et al., 2013; Zhao et al., 2016; Lin et al., 2019), and the direct discrete differentiation methods, where the hybrid inputs are the displacement term, which can be selected by discrete window function and the wave equation (Bielak et al., 2003; Masson et al., 2014). A recent review (Lyu et al., 2022) compared and analyzed the physical and numerical categories and proposed a combined way to calculate the combined hybrid inputs with the traction, displacement, and acceleration terms.

In the research on the two-step hybrid method, the accurate calculation of the equivalent forces is crucial. The accuracy of the resultant waveform in the hybrid numerical simulation is affected by the spatial and temporal dispersion errors, simulated duration, and the error of the hybrid inputs. It should be noted that the errors of the hybrid inputs are synchronously affected by the spatial interpolation when calculating the hybrid inputs with different meshing and are also affected by the temporal

interpolation when one sparsely saves the hybrid inputs but recovers them in a much smaller time step. Despite the widespread application of hybrid simulation methods in computational seismology, studies on quantitatively investigating and controlling these errors are relatively lacking.

As far as spatial interpolation is concerned, it is known that in the realistic application, the first global simulation is performed in a background reference model without complicated local small-scale geological features, and the grid size of the first global simulation is generally larger than that of the subsequent local simulations. Therefore, during the first global simulation, people usually use spatial interpolation methods to obtain displacements (or potentials in the acoustic case) of some coordinates determined by the local meshing for subsequent hybrid simulation. Previous studies (Clouzet et al., 2018; Lyu et al., 2022) adopted the Lagrange interpolation method, in which the interpolation gird is only made up of the Gauss–Lobatto–Legendre (GLL) points from one element (Figure 2). This introduces spatial error and affects the results of the local simulation, but no quantitative investigation has been conducted.

In terms of temporal interpolation, according to the Courant–Friedrichs–Lewy (CFL) stability condition, the time step of the SEM is proportional to the ratio between the shortest distance between two neighboring GLL points and the maximum velocity. Usually, due to the existence of the small-scale structures in the hybrid simulation, the time step of the global simulation is much larger than that of the local simulation and, thus, the time series of hybrid inputs (displacements or potentials) would require upsampling to perform the local simulation. Furthermore, to save memory, the hybrid inputs are often sparsely stored in the global simulation and then interpolated/recovered to a suitable time interval constrained by the local small-scale structures during the local simulation. Thus, temporal interpolation is also essential for calculating the hybrid inputs. Monteiller et al. (2021) proposed that the cubic B-spline interpolation is efficient for upsampling the hybrid inputs because it only requires two additions and two multiplications per sample point. However, this method would fail to recover the original hybrid inputs at a very high upsampling ratio (Zhang et al., 2017).

In this study, we focus on the error propagation of the two-step hybrid method in acoustic wave case, while the hybrid inputs are calculated using a slightly modified direct discrete differentiation method of Masson et al. (2014). In the spatial interpolation, the multi-elements spline spatial interpolation in 2D cases and globally spline spatial interpolation in 3D cases are proposed to calculate the hybrid inputs during the global simulation. In the temporal interpolation, the Fourier temporal interpolation method is introduced to record and recover the sparsely stored hybrid inputs during the global and local simulations. The article is arranged as follows. First, we present the theory of the two-step hybrid method and the

proposed spatial- and temporal-refinement schemes in the methodology section. Then, we verify our methods through several 2-D and 3-D hybrid numerical simulations of the acoustic wave using SEM in the numerical experiments section.

2 Methodology

In this section, we start with a brief description of the acoustic wave equation and the fundamental concept of SEM. The principle of the two-step hybrid method and the expression of the equivalent forces of the direct discrete differentiation method are then introduced. Whereafter, we introduce the Fourier temporal interpolation method into the hybrid simulation to recover the sparsely stored hybrid inputs. Finally, we propose a different spatial interpolation method, the multi-elements spline interpolation method, which is suitable for the case that the meshing of the global and local simulations differs.

2.1 Acoustic wave equation

In this study, we only discuss the error propagation of the hybrid numerical simulation of the acoustic wave equation. We consider a velocity potential field $q(\mathbf{x}, t)$ in an arbitrary acoustic domain Ω that is a solution of the acoustic wave equation

$$\begin{cases} \frac{1}{\kappa}\ddot{q} = \nabla \cdot \dot{\mathbf{u}} + f \\ \dot{\mathbf{u}} = \frac{1}{\rho}\nabla q, \end{cases} \tag{1}$$

where $\mathbf{u}(\mathbf{x}, t)$ is the displacement vector, $f(\mathbf{x}, t)$ is the source time function, $\rho(\mathbf{x})$ is the density, and $\kappa(\mathbf{x})$ is the bulk modulus. In general, an acoustic medium can be fully described by density $\rho(\mathbf{x})$ and sound speed $V(\mathbf{x})$, namely, $\kappa(\mathbf{x}) = \rho(\mathbf{x})V^2(\mathbf{x})$.

2.2 Fundamental concept of SEM

In both regional and global seismology, SEM is one of the most extensively used numerical methods to calculate seismograms in realistic Earth models (Tape et al., 2009; French and Romanowicz, 2014; Chen et al., 2015; He et al., 2015; Chen et al., 2017; Lei et al., 2020). Compared with the traditional numerical simulation methods such as FDM, which directly solves the strong form of the wave equation, SEM is implemented to solve the weak form of the wave equation. The weak form of the wave equation can be obtained by multiplying an arbitrary test function on both sides of the equation and by integrating parts over the entire domain Ω. This results in the implicit introduction of the free-surface boundary condition, which is a useful feature for dealing with the circumstance when there is surface topography in a realistic model. To calculate the

solution of the wave equation on the computer, the continuous equation must be discretized in both time and space. As in a classical finite element method (FEM), the model domain Ω is subdivided into a lot of non-overlapping elements. In each independent element, the unknown velocity potential $q^e(\mathbf{x}, t)$ can be approximated using the Lagrange approximation

$$q^e(\mathbf{x}, t) \approx \sum_{i=1}^{N} q_i^e(t)\varphi_i(\mathbf{x}), \tag{2}$$

where N is the polynomial degree (1D case as an example), $\varphi_i(\mathbf{x})$ is the basis function in the ith GLL point, and $q_i^e(t)$ is the potential at the ith GLL point in the element. In the SEM, the choice of basis function is Lagrange polynomials $l_i(\mathbf{x})$, which have an elegant orthogonality, such that $l_i(x_j) = \delta_{ij}$, where δ_{ij} is the Kronecker symbol. The collocation points used in SEM are the so-called GLL points (Komatitsch and Vilotte, 1998).

The numerical integration rule of SEM in each element is the GLL quadrature, with the GLL points serving as integral points. Let us take an example to demonstrate this integration rule. For an arbitrary continuous function $f(x)$ defined in the domain of element with $x \in [-1, 1]$:

$$\int_{-1}^{1} f(x)dx \approx \sum_{i=1}^{N+1} \omega_i f(x_i), \tag{3}$$

with

$$\omega_i = \int_{-1}^{1} l_i^{(N)}(x)dx, \tag{4}$$

where $l_i^{(N)}(x)$ is the Lagrange polynomial of degree N at the ith GLL point.

The next step is to assemble the global solution after we have specified the solution at an elemental level, and Equation (1) was converted to an ordinary differential equation (ODE), which can be expressed as

$$\mathbf{M} \cdot \ddot{\mathbf{Q}} + \mathbf{K} \cdot \mathbf{Q} = \mathbf{f}, \tag{5}$$

where $\mathbf{M}$ is the global mass matrix, $\mathbf{K}$ is the global stiffness matrix, $\mathbf{f}$ is the source vector, $\mathbf{Q}$ and $\ddot{\mathbf{Q}}$ are the unknown global velocity potential vector and its second-time derivative. It is of note that $\mathbf{M}$ is a diagonal matrix that is easy to invert and can be stored as a vector in the program. The product $\mathbf{K} \cdot \mathbf{Q}$ between global stiffness matrix $\mathbf{K}$ and potential vector $\mathbf{Q}$ is calculated by tensor product (Komatitsch and Vilotte, 1998). These terrific features result in the explicit algorithm being extremely efficient, and it can be utilized to deal with a realistic 3D Earth model.

2.3 Principle of the two-step hybrid method

The key superiority of the two-step hybrid method is that wave propagation simulation is implemented inside the local region of interest rather than the global region that encompasses

the sources and receivers. For the sake of clarity, we first specify the decomposition of the computational domain. As shown in Figure 1, the global computational domain Ω_g is separated into two parts: external domain Ω_e and local domain Ω_l bordered by hybrid interface $\partial\Omega$, such that $\Omega_g = \Omega_e + \Omega_l$. The location of sources and receivers can be arbitrary, but the situation that sources are located in the external domain Ω_e, is more meaningful as this method is used to simulate the propagation of seismic waves generated by remote events (Bielak et al., 2003).

The global waveform tomography is in pursuit for a real 3-D Earth model across the observable frequency band, the computation cost is proportional to the minimum wavelength to the fourth power, and is still computationally prohibitive nowadays because of its large computational domain. However, in the framework of the hybrid simulation, this global simulation only needs to be run a few times if the velocity structure in the external domain is assumed to be unperturbed during the iterative box tomography. The first step is to perform a forward simulation to solve and record the global wavefield $\mathbf{Q}(t)$ in the global domain Ω_g. In the second steps, wave numerical propagation is confined to the local domain Ω_l and the recorded hybrid inputs are imposed on hybrid interface $\partial\Omega$ as equivalent sources. If the local structure is the same as the reference global structure, the result of the two-step hybrid method is to regenerate a local wavefield that is identical to the wavefield generated by the global simulation. It is of note that if receivers are placed outside the local domain Ω_l, the seismic response is calculated using the wavefield extrapolation method (Robertsson and Chapman, 2000).

The key process in the two-step hybrid method is the algorithm for determining the hybrid inputs, namely, equivalent forces described earlier, which are imposed into the local model to perform the local simulation. We adopted the conceptual framework proposed by Masson et al. (2014) to construct the equivalent forces. This method was proposed by introducing a spatial window function on a discrete wave equation. When we obtained the origin wavefield $\mathbf{Q}(t)$ by solving Equation (5) within the global domain during the first simulation, the hybrid wavefield (the temporal wavefield in the local simulation) $\mathbf{Q}^L(t)$ can be written as

$$\mathbf{Q}^L(t) = \mathbf{W} \cdot \mathbf{Q}(t), \qquad (6)$$

where $\mathbf{W}$ is a diagonal matrix of window function w. The window function w is equal to one inside the local domain Ω_l and on the hybrid interface $\partial\Omega$, and zero outside, as shown in Figure 1. The equivalent forces $\mathbf{f}^L$ can be explicitly expressed as (Masson et al., 2014)

$$\mathbf{f}^L = \mathbf{W} \cdot \mathbf{f} - \mathbf{W} \cdot (\mathbf{K} \cdot \mathbf{Q}) + \mathbf{K} \cdot (\mathbf{W} \cdot \mathbf{Q}), \qquad (7)$$

or

$$\mathbf{f}^L = \mathbf{W} \cdot \mathbf{f} + (\mathbf{I} - \mathbf{W}) \cdot (\mathbf{K} \cdot \mathbf{Q}) - \mathbf{K} \cdot [(\mathbf{I} - \mathbf{W}) \cdot \mathbf{Q}]. \qquad (8)$$

We note that $\mathbf{f}^L$ in Equation 7 and Equation 8 are the discrete expressions of the equivalent forces, and they can be constructed only by the selected physical quantity Q, namely, the hybrid inputs in this study. In SEM, the computational domain consists of many elements. Therefore, when getting down to the element level, Equation (7) becomes

$$\mathbf{f}^L = \sum_e \mathbf{W}_e \cdot \mathbf{f}_e + \mathbf{W}_e \cdot (\mathbf{K}_e \cdot \mathbf{Q}_e) - \mathbf{K}_e \cdot (\mathbf{W}_e \cdot \mathbf{Q}_e), \qquad (9)$$

and Equation (8) becomes

$$\mathbf{f}^L = \sum_e \mathbf{W}_e \cdot \mathbf{f}_e + (\mathbf{I} - \mathbf{W}_e) \cdot (\mathbf{K}_e \cdot \mathbf{Q}_e) - \mathbf{K}_e \cdot [(\mathbf{I} - \mathbf{W}_e) \cdot \mathbf{Q}_e]. \qquad (10)$$

Here, $\mathbf{Q}_e$, $\mathbf{K}_e$, $\mathbf{f}_e$, and $\mathbf{W}_e$ are the locally elemental potential vector, stiffness matrix, source vector, and window function, respectively. The local window function $\mathbf{W}_e$ can be written as

$$\mathbf{W}_e = \begin{pmatrix} w_e^1 & \cdots & 0 \\ \vdots & \ddots & \vdots \\ 0 & \cdots & w_e^{N_\varphi} \end{pmatrix}, \qquad (11)$$

where N_φ is the number of the GLL points in each element. As mentioned earlier, the value of w_e^i is equal to one inside the local domain and on the hybrid interface, and zero outside. In general, the source term $\mathbf{W}_e \cdot \mathbf{f}_e$ is zero as the sources are usually placed outside the local domain in remote events, in which its window function $\mathbf{W}_e$ is zero. In addition, for elements with a constant window function $\mathbf{W}_e = \alpha\mathbf{I}$, the last two terms in Equations (9), (10) are canceled out of each other. Thus, only the non-constant window function $\mathbf{W}_e$, named by the "hybrid elements" crossed by the hybrid interface $\partial\Omega$, has contributed to the equivalent forces $\mathbf{f}^L$. Therefore, implementing the hybrid simulation using SEM does not need to record origin wavefield at all GLL points in the complete domain during the global simulation. According to the inner scheme in Equation (9), we only need the values of the internal forces, $\mathbf{K}_e \cdot \mathbf{Q}_e$ and $\mathbf{K}_e \cdot (\mathbf{W}_e \cdot \mathbf{Q}_e)$, at the part of the GLL points of hybrid elements inside the local domain. In contrast, if we use the outer scheme in Equation (10), the GLL points of hybrid elements outside the local domain are required (Masson et al., 2014).

2.4 Fourier interpolation in time domain

In order to save the memory requirements, the hybrid inputs obtained during the global simulation are usually stored on disk at a relatively large time interval because the stable time steps used in numerical simulation generally are much smaller than the Nyquist sampling limit. As the time step of the local simulation, in the best case, is completely independent of the global time step. In the local simulation, the hybrid inputs are then interpolated/recovered to a suitable time step for a local target structure. However, the traditional spline interpolation method

(Monteiller et al., 2021) would fail at high upsampling ratios, as shown by Zhang et al. (2017). In this section, we introduce a new scheme for sampling and saving the hybrid inputs in the time domain using the Fourier interpolation method (Schafer and Rabiner, 1973).

For a discrete time series $x[n]$, $n = 0, 1, \cdots, N - 1$ its Fourier transform is defined as (Sacchi et al., 1998)

$$X[k] = \sum_{n=0}^{N-1} x[n]e^{-i2\pi nk/N}, \quad k = 0, 1, \cdots, N - 1, \quad (12)$$

where $i = \sqrt{-1}$, N is the total length of time series. The inverse Fourier transform is defined as

$$x[n] = \frac{1}{N} \sum_{k=0}^{N-1} X[k]e^{i2\pi nk/N}, \quad n = 0, 1, \cdots, N - 1. \quad (13)$$

Assuming that the time step of the simulation is Δt, we store the origin wavefield $\mathbf{q}(t)$ with time step $M\Delta t$ during the global simulation, where M is an integer which we name the upsampling ratio. We record this rough time series as $x[n]$ that satisfies

$$x[n] = \mathbf{q}(n \cdot M\Delta t), \quad n = 0, 1, \cdots N - 1. \quad (14)$$

A new time series $y[n]$ is obtained with time step Δt, having a total length $M \cdot N$ that satisfies

$$y[n] = \mathbf{q}(n \cdot \Delta t), \quad n = 0, 1, \cdots, MN - 1. \quad (15)$$

For the convenience of subsequent discussion, here, we introduce and define the meaning of a special superscript n^+, thus,

$$n^+ = n \ (n \ \text{even}), \quad n^+ = n + 1 \ (n \ \text{odd}). \quad (16)$$

Since the sequence $x[n]$ only supplies values of the required sequence $y[n]$ at the interval of $M\Delta t$, the remaining samples must be filled in by interpolation. From the point of view of digital signal processing, there is a clear relationship between the amplitude spectrum of these two sequences (Fraser, 1989). The first half of the amplitude spectrum of $y[n]$ can be expressed by the amplitude spectrum of sampling series $x[n]$ as

$$Y[k] = \begin{cases} X[k], & k = 0, 1, \cdots, \dfrac{N^+}{2} - 1 \\ 0, & k = \dfrac{N^+}{2}, \dfrac{N^+}{2} + 1, \cdots, \dfrac{MN^+}{2} - 1, \end{cases} \quad (17)$$

and the other half can be easily obtained from the first half because the amplitude spectrum of a signal is symmetrical at the Nyquist frequency. Once we have the amplitude spectrum $Y[k]$, we can easily obtain its time series $y[n]$ using inverse Fourier transform in Equation (13). We can now see that inserting zeros in the frequency domain at the Nyquist frequency is equivalent to decreasing the time step in the time domain, which is the key idea of the Fourier interpolation.

The requirement for the Fourier interpolation is that the waveform generated by numerical simulation is band-limited, which has no abrupt jump or discontinuity, and the rough sampling series $x[n]$ satisfies the sampling theory (Oppenheim et al., 1999). This means that the maximum non-zero frequency component of band-limited wavefield would below the Nyquist limit to avoid the aliased spectral leakage; in other words, the amplitude spectrum must equal to zero around the Nyquist frequency. According to Zhang et al. (2017), this requirement can be met by applying a smooth tapering window. Thus, the rough sampling series $x[n]$ will be multiplied by a smooth window function (eg., Hanning window) to ensure that the wavefield is periodic, which will improve the accuracy of the Fourier interpolation even further. It should also be noted that the hybrid inputs used in this study is the time series of potential, which is frequency-banded, so the tapering process is only needed at the ending part of the stored potential series.

In practice, the workflow of the Fourier interpolation method for recovering hybrid inputs in the time domain consists of the following four main steps: (a) Applying a smooth window tapering window function (Hanning window used in this study) to the time series of the hybrid inputs; (b) performing a forward Fourier transform; (c) inserting (M-1)·N zeros at the Nyquist frequency; and (d) performing an inverse Fourier transform. Thus, the main complexity of the algorithm is the Fourier transform. In this study, we use the mature MATLAB built-in function *fft/ifft*, which is based on the fast Fourier transform algorithm and is compatible with double precision data.

2.5 Multi-elements spline interpolation method

In the process of box tomography, the global simulation is implemented in a 3D reference model with long wavelength (large-scale) structures. The grid size is only decided by the long wavelength. In subsequent local simulations, the model alterations at each iteration are confined within the local domain with the small-scale structures. To improve imaging resolution in the local domain, it is advisable to reduce the grid size in the local domain during the local simulations. In general, two different solvers are used for the global and local simulations, and their corresponding spatial meshing is usually inconsistent. A recent study by Clouzet et al. (2018) showed that the Lagrange interpolation method can be used to determine the hybrid inputs at the GLL nodes of a local meshing different from the global meshing. However, this method introduces spatial-interpolation error into the hybrid inputs used to regenerate the hybrid wavefield. In this subsection, we propose an improved spatial interpolation method that can effectively suppress this spatial-interpolation error.

Considering the case where the meshing of the global and local simulations differs, as pictured in Figure 2. According to Equation (10), to obtain the equivalent forces to perform the local simulation, we need to know the wavefield values **Q** at all the GLL nodes in the hybrid elements. However, after finishing the first global simulation, we only know the wavefield values **Q** at coarse GLL nodes (the diamond symbol). Thus, we need to interpolate the wavefield from the coarse grid to the fine grid.

In SEM, it is natural to use the Lagrange interpolation since the interpolation weights at the GLL points of each global element are already known during the first global simulation. For example, as pictured in Figure 2, if we wish to interpolate the wavefield at the red point in the bottom right corner of the local domain, we need to find the values of the wavefield and weights at the GLL points within its corresponding global element (the blue solid diamonds), similar to computing the displacement for the station with any location. A problem with the Lagrange interpolation method is that only several GLL points within the single global element are used as interpolation points. This will affect the accuracy of the hybrid inputs, especially for the lower polynomial degree SEM, and these inaccurate hybrid inputs will lead to the hybrid waveform with large errors after accumulation in the local simulation because we need to repeatedly impose the hybrid inputs in each global forward simulation during the iterative box tomography, and finally, this error will be transferred to the inverted velocity structures.

We find that using more elements as the interpolated grid for calculating hybrid inputs can efficiently reduce this spatial error. For example, as shown in Figure 2, for a red point in the top left corner to be solved, we construct an interpolation grid that consists of GLL points from its corresponding global element and the neighboring elements (the cyan solid diamonds), and the spline interpolation method is used to calculate the wavefield values.

The cubic Bi-cubic spline interpolation is useful to solve a surface fitting problem for 2D data, which is consist of third-order polynomial pieces in grid squares. The intuitive explicit form of a third-order polynomial function can be written as (Hayes and Halliday, 1974)

$$f(x, y) = \sum_{i=0}^{3} \sum_{j=0}^{3} a_{ij} x^i y^j, \qquad (18)$$

with 16 unknown coefficients a_{ij}, $i, j = 0, 1, 2, 3$. To obtain the general representation of the spline function in the whole range of data points, we need to construct a set of basis functions $M_i(x)$ in x direction with respect to the knots $\lambda_1, \lambda_2, ..., \lambda_h$, and a set of basis functions $N_j(y)$ in y direction with respect to the knots $\mu_1, \mu_2, ..., \mu_k$. These basis functions are non-zero only when $\lambda_i < x < \lambda_{i+1}$ and $\mu_j < y < \mu_{j+1}$. Then, the general spline function is represented as

$$s(x, y) = \sum_{i=1}^{h} \sum_{j=1}^{k} \beta_{ij} M_i(x) N_j(y), \qquad (19)$$

where β_{ij} is the unknown coefficients determined by wavefield values $q_r(x_r, y_r)$, $r = 1, 2, ..., n$, at all GLL points in the constructed interpolation grid. In the 2D case, the interpolation grid of the new method uses nine elements, one of which contains the target point, and the others are surrounding elements, and the number of GLL points is determined by the orders of SEM. The basis function can be calculated using the Cox de Boor recursion formula (Cox, 1972)

$$M_{1i}(x) = \begin{cases} 1/(\lambda_i - \lambda_{i-1}), & \text{if } \lambda_{i-1} \le x < \lambda_i \\ 0, & \text{otherwise,} \end{cases} \qquad (20)$$

$$M_{pi}(x) = \frac{(x - \lambda_{i-p}) M_{p-1,i-1}(x) + (\lambda_i - x) M_{p-1,i}(x)}{\lambda_i - \lambda_{i-p}}, \qquad (21)$$

where M_{pi} is the B-spline basis function of degree $(n-1)$, so that $M_{4i}(x)$ is the basis function $M_i(x)$ in cubic spline interpolation. Then, substituting the known wavefield values $q(x_r, y_r)$ into Equation (19), the coefficients β_{ij} can be calculated by solving the linear equations

$$\sum_{i=1}^{h} \sum_{j=1}^{k} \beta_{ij} M_i(x_r) N_j(y_r) = q_r, \quad r = 1, 2, ..., n. \qquad (22)$$

This can be written in the linear matrix system as

$$\mathbf{A}\boldsymbol{\beta} = \mathbf{q} \qquad (23)$$

where **A** is a bandwidth matrix with the dimension of (n, hk). Because n is substantially bigger than hk, the linear system in Equation (23) is over-determined; thus, this is equivalent to finding the least square solution to the over-determined system

$$\mathbf{A}^T \mathbf{A} \boldsymbol{\beta} = \mathbf{A}^T \mathbf{q}. \qquad (24)$$

where $\mathbf{A}^T \mathbf{A}$ has a symmetric and banded structure that can be efficiently factorized and stored. Once the spline coefficients are calculated, the wavefield values of local GLL points can be easily determined using Equation (19). It is of note that a similar method has been used in time direction illustrated in the appendix in Sevan 2022 (under review).

Our new method has the advantage of having more polydirectional interpolation points in the interpolation grid, which allows the wavefield values at local GLL points to be better constrained in each direction, resulting in more accurate hybrid inputs for local simulations. To distinguish it from the traditional Lagrange interpolation method, we refer to this new method as the multi-elements spline interpolation (MSI) method.

In practice, if we solve the spline coefficients point by point over the hybrid elements, the computational cost is exceedingly large because we must repeatedly reconstruct the interpolation grid and compute the spline coefficients for each point and time step, especially in the 3D case. Another alternative method used

in this study is to solve all of the points in the hybrid elements at once. The interpolation grid of this method consists of the total elements in the local domain and an additional layer of elements that encompass the local domain. This interpolation grid can be used to compute all the GLL points associated with the hybrid inputs, and, thus, the spline coefficients only need to be computed once in the global simulation. In this study, the spline coefficients are computed using the MATLAB built-in function *griddedInterpolant*, which can be used for N-D gridded data sets and has double precision.

3 Numerical experiments

To verify the accuracy of the proposed interpolation methods in spatial and time domains on the saving and recovery of the hybrid inputs, we conduct a series of hybrid numerical simulations using SEM in both 2D homogeneous and heterogeneous models, as well as 3D PREM model. In all numerical experiments, both the initial velocity potential q and its first-time derivative $\dot{q}$ are zero. It is of note that the local model perturbations are set to zero in this study to focus on the accuracy of the hybrid inputs. This means that if the hybrid method is theoretically exact, the results of the global and local simulations are equal. If they are different, their difference is the error. Following the error measurement method described by Lyu et al. (2020), the hybrid method error E is computed as

$$E^2 = \frac{\int_0^{t_{\max}} (\mathbf{q}^L(t) - \mathbf{q}^G(t))^2 dt}{\int_0^{t_{\max}} (\mathbf{q}^G(t))^2 dt} \qquad (25)$$

where $\mathbf{q}^L(t)$ and $\mathbf{q}^G(t)$ are the velocity potential calculated in the local and global simulations, respectively. In a hybrid numerical simulation, we define the *residual waveform* as the waveform difference between the global simulation and its corresponding local simulation. It is of note that we use the waveform obtained from the global simulation as the reference (not the pure accurate numerical waveform in Lyu et al. (2020)) because the target of hybrid simulation is to get the hybrid waveforms to be as similar to the global simulation as possible.

In the temporal interpolation experiment, we keep the same meshing and time step in the global and local simulations, while the hybrid inputs are sparsely stored in disk and then recovered to the same time step as the local simulation using the temporal interpolation method. The temporal interpolation experiment is mainly carried out in two steps. First, we calculate and store the hybrid inputs with the same time step as the local simulation and take the result of this hybrid simulation as a reference. In the second step, we calculate and store the hybrid inputs with a large time interval during the global simulation. Then, we use the different temporal interpolation methods (spline and Fourier interpolation methods) to recover them during the local simulation and compare the results to the reference result. As

we use the same meshing and time step in the global and local simulations, the temporal and spatial dispersion errors of the hybrid simulation will cancel out (see a detailed demonstration in Section 3.1.1). There are no additional spatial errors because the hybrid inputs can be directly obtained without the need for spatial interpolation. Therefore, the errors of the hybrid simulation are only caused by inaccurate hybrid inputs due to temporal interpolation.

In the spatial interpolation experiment, we keep the same time step in both the hybrid simulation and stored hybrid inputs to eliminate temporal error and dispersion. We use different meshing in the global and local simulations, and the hybrid inputs in the local GLL points are calculated using the traditional Lagrange interpolation and proposed MSI method, respectively. Therefore, there are two sources of errors: different spatial dispersions in the global and local simulations and inaccurate hybrid inputs calculated using spatial interpolation.
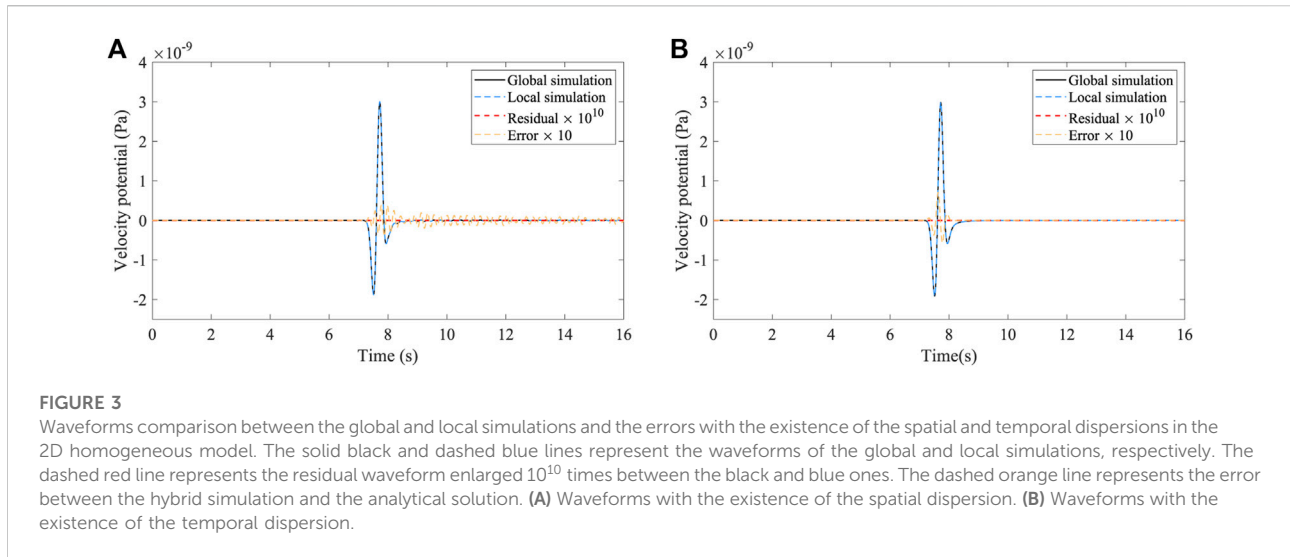
3.1 2D hybrid numerical simulations in the homogeneous model

In the 2D homogeneous model, we set a constant P wave velocity V_p = 3750 m/s and density ρ = 2000 kg/m³. The size of the global model is 100×50 km and the size of the local model is 20×10 km, which is located at the center of the global model. The source time function is a Ricker wavelet with a dominant frequency of *2* Hz (maximum frequency is about 6 Hz) and located at the surface center. The receiver is located at the center of the model and it is overlapped with one GLL point so that there is no extra error attributed to wavefield interpolation.

3.1.1 Accuracy of the two-step hybrid method

To validate the accuracy of the two-step hybrid method of Masson et al. (2014) in the presence of spatial- and temporal-dispersion errors, which are inherent characteristics generated by numerical approximation (Igel, 2017), we perform three hybrid numerical simulations with different spatial grids and time steps. We keep the same meshing between the global and the local domains, which means that the GLL points of the local domain are exactly overlapped with the global ones.

First, we perform a global simulation with meshing $160 \Delta x \times 80 \Delta z$, where $\Delta x = \Delta z = 625$ m is the length of the element in x and z orthogonal directions, with nine GLL points per direction (the number of points per minimum wavelength "G" value is about 8), and time step $\Delta t =$ 0.00125 s (Courant number is equal to 0.15); this produces relatively little spatial and temporal dispersion errors and we take it as the analytical solution of the model. Then we perform global and local simulations that only changes the meshing to $60 \Delta x \times 30 \Delta z$, where $\Delta x = \Delta z \approx 1667$ m, and other parameters remain invariable. Figure 3A shows the waveforms of the global simulation and associated local simulation and their residual

FIGURE 3
Waveforms comparison between the global and local simulations and the errors with the existence of the spatial and temporal dispersions in the 2D homogeneous model. The solid black and dashed blue lines represent the waveforms of the global and local simulations, respectively. The dashed red line represents the residual waveform enlarged 10^{10} times between the black and blue ones. The dashed orange line represents the error between the hybrid simulation and the analytical solution. **(A)** Waveforms with the existence of the spatial dispersion. **(B)** Waveforms with the existence of the temporal dispersion.

waveform, which is the difference between these two simulations. In addition, compared with the analytical solution, this simulation has certain spatial dispersion error due to its larger grid (the orange dash line). In the next hybrid simulation, we only change the time step to $\Delta t = 0.005s$ (Courant number is equal to 0.6), both in the global and local simulations, while other parameters are the same as the ones in the analytical solution. Therefore, the error between this simulation and the analytical solution is produced by temporal dispersion, as shown in Figure 3B.

We can see that although the spatial and temporal dispersion existed in the numerical simulation, the residual waveforms of the hybrid simulation are constantly zeros even if they are enlarged by the factor of 10^{10} times. This means that if the meshing of the global and local simulations is the same, the hybrid waveform of Masson et al. (2014) is always the same as the global simulation, however with the same spatial- and temporal-dispersion errors.

3.1.2 Validation and comparison of the Fourier interpolation method with a traditional method
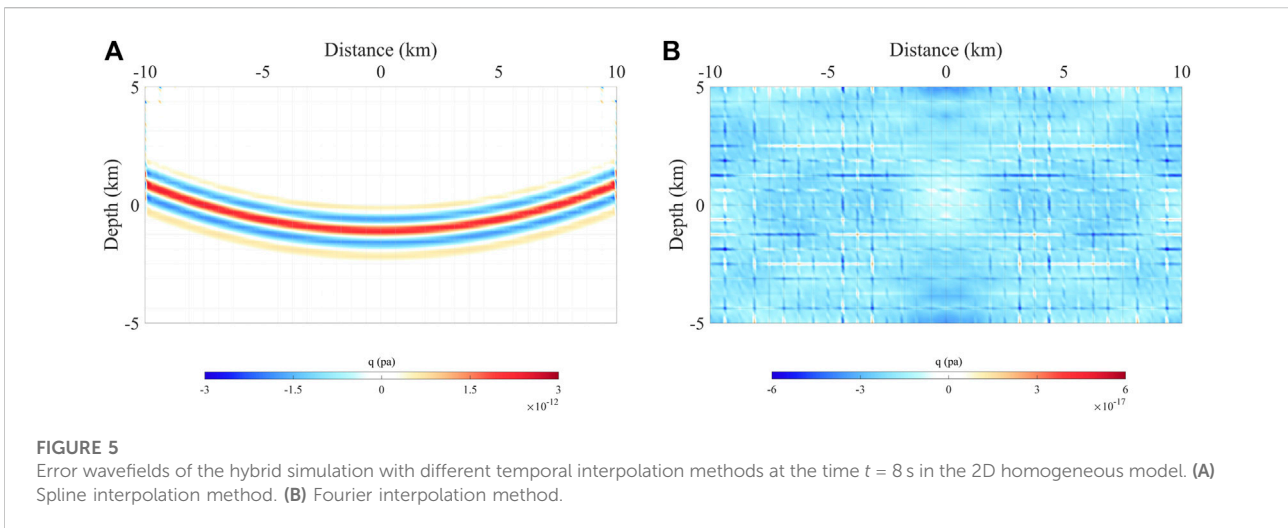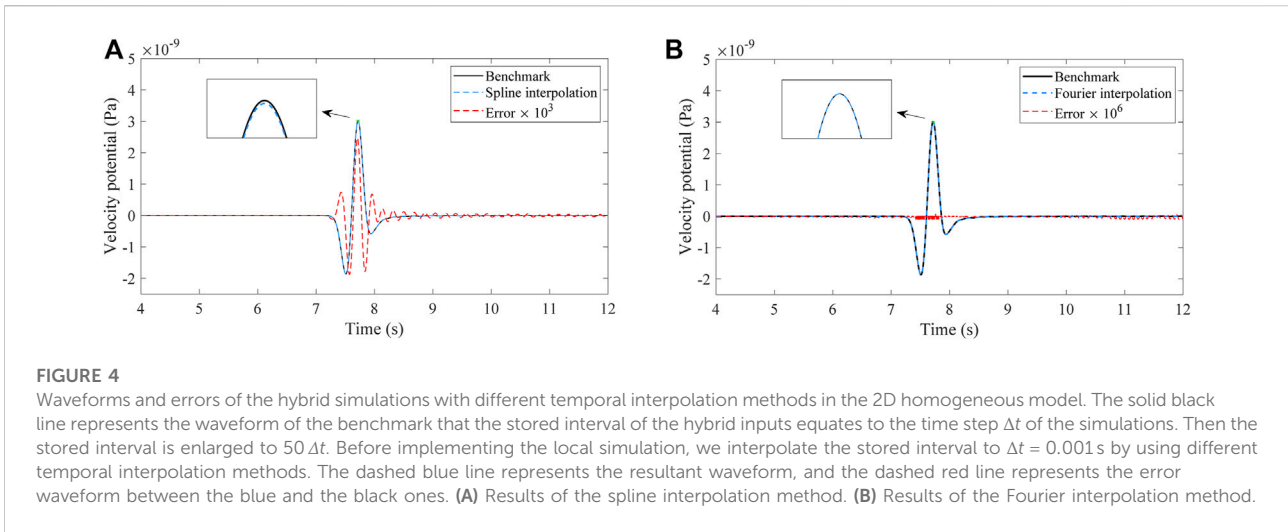
We verified the accuracy of the Fourier interpolation in the time domain and compared it with the traditional spline interpolation to illustrate the improvement that can be achieved. To avoid the effect of the spatial errors caused by different meshing, we set the global and local domains with the same grid size of $\Delta x = \Delta z = 625$ m with five GLL points per direction. Thus, there are 160×80 elements in the global domain and 32×16 elements in the local domain. The time step is $\Delta t = 0.001$ s both in the global and local simulations, and the total duration is $12000\,\Delta t$.

First, we store the hybrid inputs with a time interval of 0.001 s, which is equal to the time step Δt of the global simulation. Then, we can directly implement the local simulation without

any interpolation for the hybrid inputs. We take the results of this simulation as a reference, and then we increase the stored interval to $50\,\Delta t$. Before implementing the local simulation, the hybrid inputs are recovered to the original time step Δt using the spline and the Fourier interpolation methods, respectively.

Figure 4 shows the resultant waveforms of different interpolation methods at upsampling ratio $M = 50$ and the errors relative to the benchmark (reference waveform). It is of note that the error of the Fourier interpolation is enlarged 10^6 times, while the error of the spline interpolation is enlarged 10^3 times. Obviously, the traditional spline interpolation method is worse than the Fourier interpolation according to the benchmark, especially on the waveform peaks. The error for Fourier interpolation is about three orders of magnitude smaller than the traditional spline interpolation, and it is distributed evenly across the entire simulation time. Figure 5 shows their error wavefields in the local model at the time of $t = 8$ s. We find that the error distribution of the spline interpolation method is consistent with the wave propagation, whereas the error of the Fourier interpolation method is distributed evenly on the entire domain.

We based on the error ratio, the ratio of maximum error of the spline interpolation method to the Fourier interpolation method, as a proxy of the improvement of the Fourier interpolation method. We also test the error of these two interpolation methods at different upsampling ratio of $M = 10, 20, \cdots, 100$, as shown in Figure 6. We can see that the error ratio reaches the peak at $M = 60$ and the errors of the Fourier interpolation have improved by about four orders of magnitude over the spline interpolation. However, the total errors of the spline interpolation method increase abruptly and become unstable at $M = 60$. When the upsampling ratio exceeds 60, the total errors of the Fourier interpolation method increase abruptly and reach the same magnitude as the Lagrange

FIGURE 4
Waveforms and errors of the hybrid simulations with different temporal interpolation methods in the 2D homogeneous model. The solid black line represents the waveform of the benchmark that the stored interval of the hybrid inputs equates to the time step Δt of the simulations. Then the stored interval is enlarged to $50 \Delta t$. Before implementing the local simulation, we interpolate the stored interval to $\Delta t = 0.001$ s by using different temporal interpolation methods. The dashed blue line represents the resultant waveform, and the dashed red line represents the error waveform between the blue and the black ones. **(A)** Results of the spline interpolation method. **(B)** Results of the Fourier interpolation method.

FIGURE 5
Error wavefields of the hybrid simulation with different temporal interpolation methods at the time $t = 8$ s in the 2D homogeneous model. **(A)** Spline interpolation method. **(B)** Fourier interpolation method.

interpolation method when the upsampling ratio exceeds the Nyquist limit. In addition, as both the errors of the Fourier and spline interpolation methods have gradually increased with upsampling ratio, it is advisable to select a suitable upsampling ratio based on resolution requirement.

3.1.3 Validation and comparison of the MSI method with a traditional method

For the case that the meshing of the global simulation differs from the local simulation, we run two hybrid numerical simulations in which the hybrid inputs are calculated by using the traditional Lagrange interpolation and proposed MSI method, respectively. For the MSI method, to test the influence of the number of interpolation grid points on the error, we consider two end-member models: (a) the interpolation grid consists of all of the elements in the local

domain as well as an additional layer of elements that encompass the local domain; (b) the interpolation grid consists of all of the elements in the global domain. The meshing of the global domain is $160 \Delta x \times 80 \Delta z$, where $\Delta x = \Delta z = 625$ m, with five GLL points per direction, and the meshing of the local domain is $320 \Delta x \times 160 \Delta z$, where $\Delta x = \Delta z = 62.5$ m, with three GLL points per direction (G value is about 20 (160×2+1)/16). The time step of these two hybrid simulations by the Lagrange interpolation and proposed MSI method is the same $\Delta t = 0.0025$ s. It is worth noting that the first global waveform of these two hybrid simulations is identical.

Figure 7 shows the resultant waveforms of these two hybrid simulations and the corresponding residual waveforms. We can see that the resultant waveforms of the local simulation are not fully correct when the meshing of the global and local domains differs. According to Equation (25), the total error of the
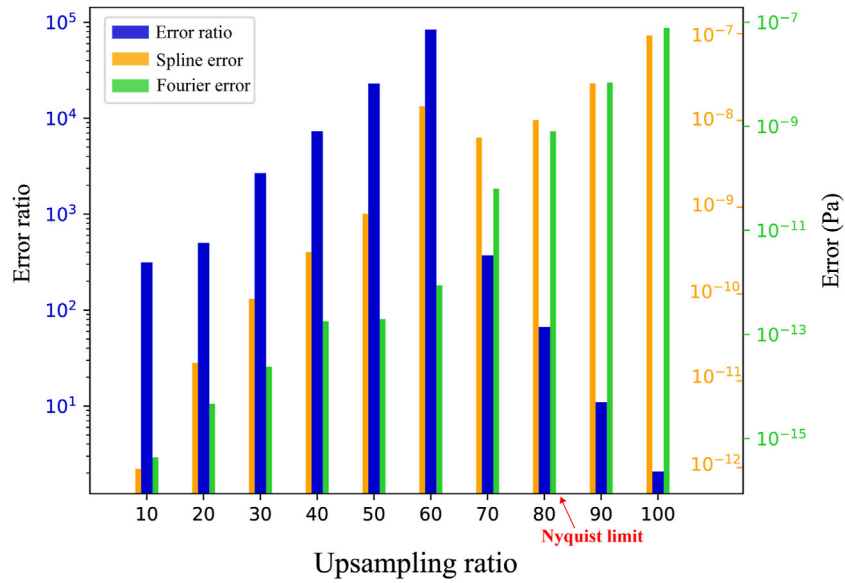
FIGURE 6
Bar chart showing the error of the spline and Fourier interpolation methods and their error ratio at different upsampling ratios of
$M = 10, 20, \cdots, 100$. The blue bar represents the error ratio, which is the ratio of maximum relative error of the spline interpolation method to the
Fourier interpolation method. The orange and green bars represent the total relative error of the spline and the Fourier interpolation methods,
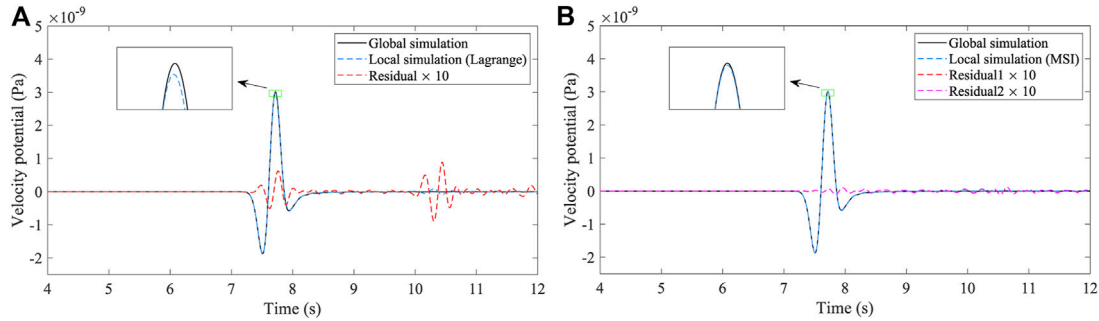respectively.

FIGURE 7
Waveform comparison of the two different spatial interpolation methods in the 2D homogenous model. The solid black and dashed blue lines
represent the waveforms of the global and local simulations, respectively. The dashed red line represents their enlarged residual waveform. **(A)**
Results of the Lagrange interpolation method. **(B)** Results of the multi-elements spline interpolation (MSI) method. *Residual1* presents the error of the
MSI method that the interpolation grid consists of all of the elements in the local domain and an additional layer of elements that encompass the
local domain. *Residual2* presents the error of the MSI method that the interpolation grid consists of all of the elements in the global domain.

traditional Lagrange interpolation method is E=5.3%, while the
total error of the MSI method is E=0.9%. This error is caused by
spatial dispersion and inaccurate hybrid inputs. Though spatial
dispersion is inevitable due to different meshing, the proposed
MSI method can effectively reduce the spatial error by improving
the calculation accuracy of hybrid inputs. Furthermore, the
nearly identical errors of the two interpolation grids for the

MSI method imply that the accuracy of the hybrid inputs is
mainly constrained by its neighboring elements. Thus, it is not
necessary to use more elements to improve the accuracy of the
MSI method, which would increase the computational cost.
Figure 8A shows the resultant wavefield of the global
simulation at $t = 8$ s, while **Figures 8B and C** show the
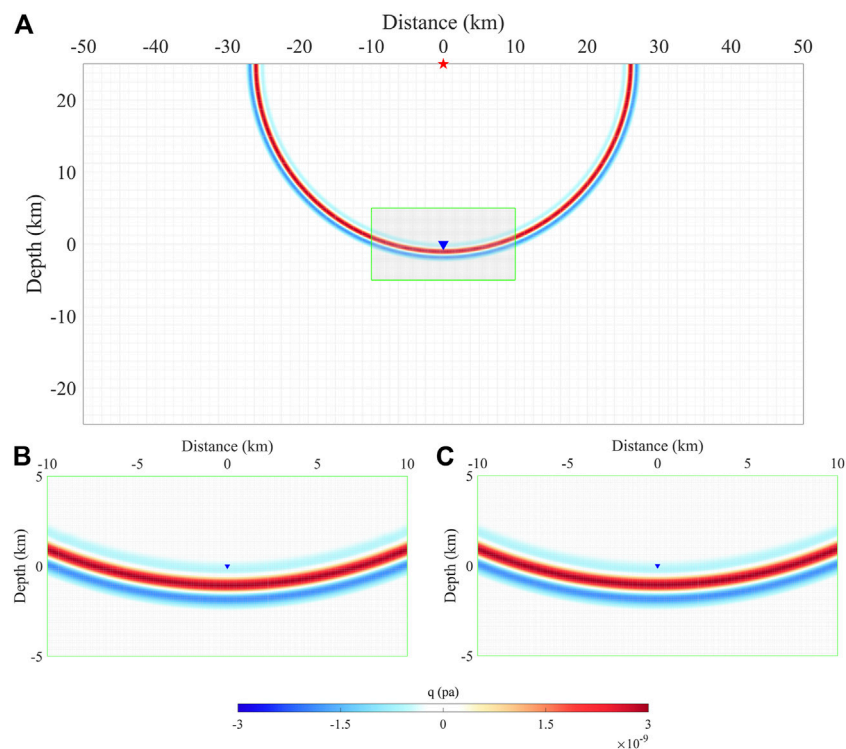wavefields of the local simulations in which the hybrid inputs

FIGURE 8
Wavefields of the global and local simulations in the 2D homogeneous model with different meshing. **(A)** Wavefield of the global simulation at
$t = 8$ s. The red star and blue triangle indicate the positions of the source and receiver, respectively. The green box represents the boundary of the
local domain. The background grid corresponds to the elements of SEM. **(B)** Wavefield of the local simulation calculated using the Lagrange
interpolation method at $t = 8$ s. **(C)** Wavefield of the local simulation calculated using the MSI method at $t = 8$ s.

are computed using Lagrange interpolation and MSI,
respectively. These two wavefields of the local simulations are
nearly identical and correspond to the local parts of the global
simulation (wavefield within the green box in Figure 8A).

3.1.4 The combination of the spatial- and temporal-interpolation methods

We applied the two temporal interpolation methods when
the global and local meshing differs, which also necessitates
the use of spatial interpolation methods to calculate the hybrid
inputs. To test the overlapped effect of the spatial errors on
temporal interpolation methods, we set two models with
different global meshing. In the first model, the meshing of
the global domain is $160 \Delta x \times 80 \Delta z$, where $\Delta x = \Delta z = 625$ m,
with eight GLL points per direction, and the meshing of the
local domain is $320 \Delta x \times 160 \Delta z$, where $\Delta x = \Delta z = 62.5$ m,
with three GLL points per direction. In the second model,
we only change the number of GLL points in the global
domain to five GLL points per direction, resulting in larger
spatial errors than the first model, while other model
parameters remain unchanged. The time step is $\Delta t =$
0.0025 s both in the global and local simulations.

In each model, the workflow is the same. In the first global
simulation, we calculated the hybrid inputs using spatial
Lagrange and MSI methods, respectively, and sparsely
stored them with the time interval of $20 \Delta t$. Then these two
stored hybrid inputs are recovered to their original time step
Δt using the temporal spline and the Fourier interpolation
methods, respectively. We now have four hybrid inputs with
different spatial- and temporal-interpolation combinations,
and we can run four local simulations with these hybrid
inputs.

Figures 9A and B show the error waveforms of these local
simulations relative to the first global simulation in the first
model (relatively small spatial errors). The errors of
traditional spline interpolation in the time domain
(Figure 9A) are relatively large, and there is no discernible
difference between the spatial Lagrange and MSI methods,
implying that the temporal errors are dominant. In contrast,
using the Fourier interpolation method in the time domain
produces relatively small errors (Figure 9B), and the
proposed spatial MSI method can further reduce the
errors. However, in the second model, for the case that
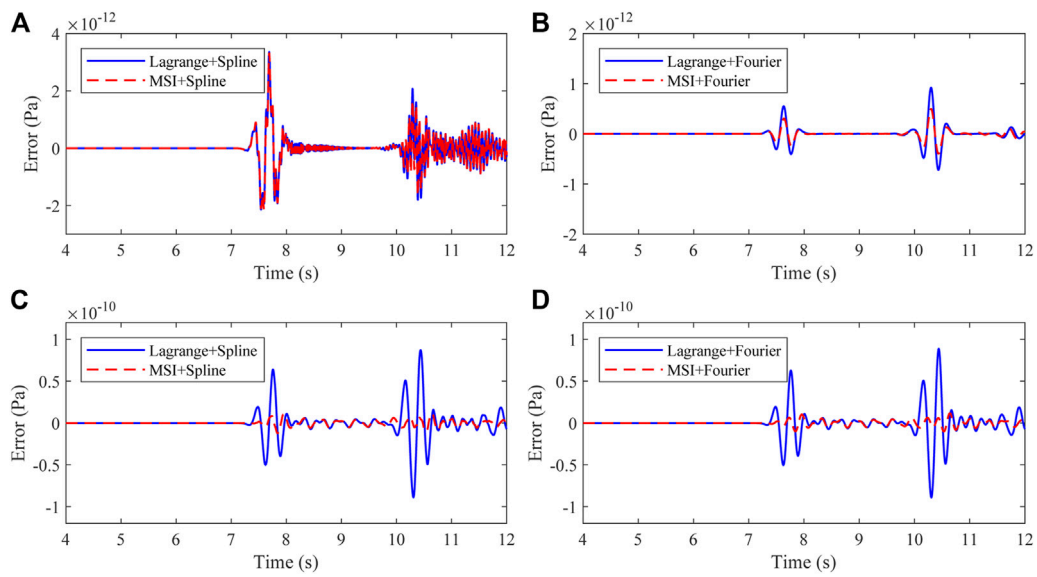the spatial errors are too large, the results of different

FIGURE 9
Error waveforms of hybrid simulations with different spatial- and temporal-interpolation methods. **(A and B)** The results in the model with eight GLL points per direction. **(C and D)** The results in the model with five GLL points per direction.
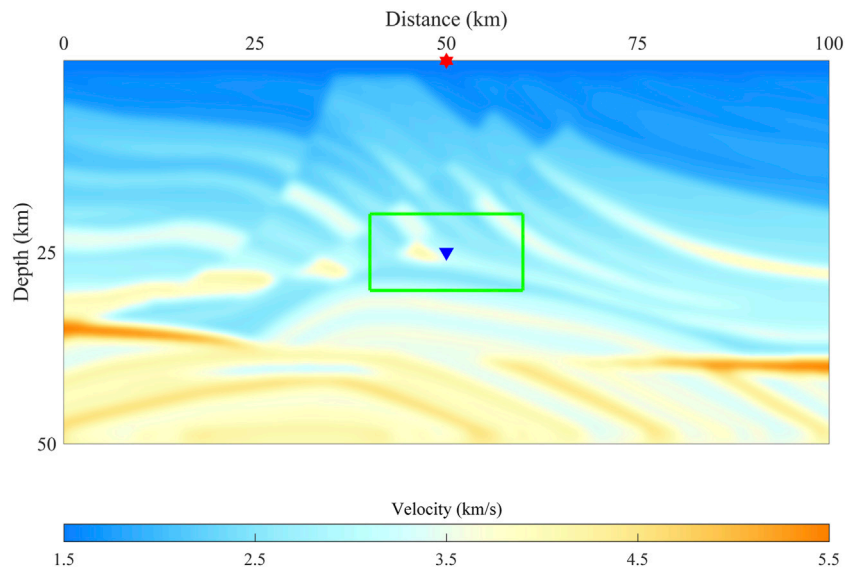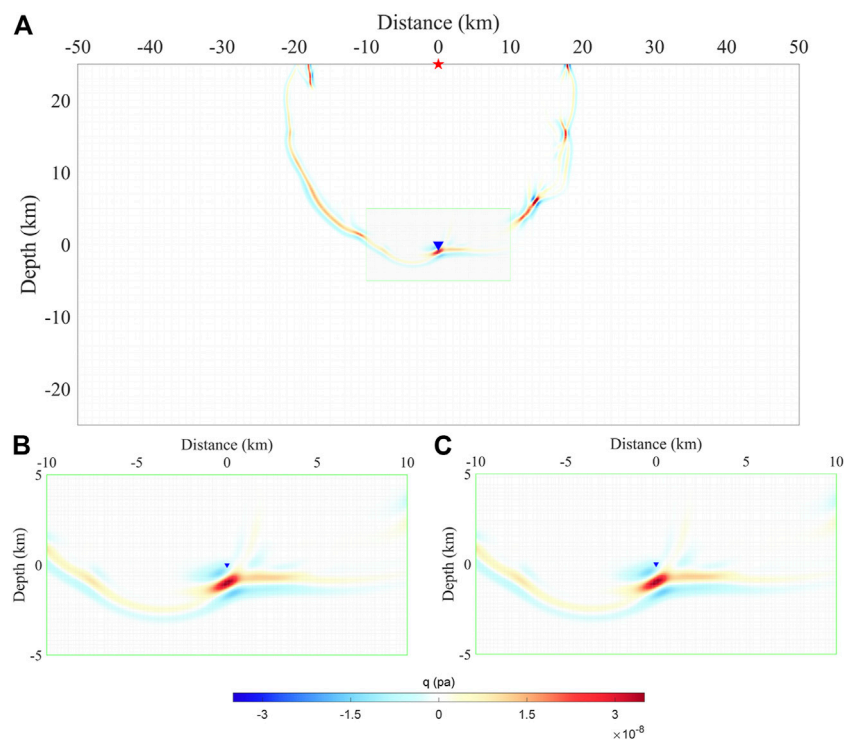

FIGURE 10
Marmousi velocity model. The red star indicates the source, the blue triangle indicates the receiver, and the green box indicates the boundary of the local model.

temporal interpolation methods are almost the same (Figures 9C and D); this means that the spatial errors are dominant, and the errors induced by time interpolation can be negligible. Thus, because the

temporal interpolation method cannot reduce spatial errors, we must ensure that the stored hybrid inputs calculated using spatial interpolation methods are as accurate as possible.

FIGURE 11
Wavefields of the global and local simulations in the 2D Marmousi model with different meshing at *t* = 13 s. **(A)** Wavefield of the global simulation. **(B)** Wavefield of the local simulation calculated using the Lagrange interpolation method. **(C)** Wavefield of the local simulation calculated using the MSI method.

3.2 Validation of the MSI method in heterogeneous model

To test the stability of the proposed spatial interpolation method, the MSI method, in a complex medium, we keep a constant density $\rho = 2000$ kg/m^3 and only change the velocity distribution to represent the heterogeneous model. We use the 2D Marmousi velocity model as our heterogeneous model, as shown in Figure 10. The target of the box tomography is to detect small-scale (10–100 km) geological structures buried in the deep Earth with seismic data from remote events and stations, such as probing the ultra-low velocity zones (ULVZ) above the core mantle boundary. To approach the case of large-scale detection, we stretch the Marmousi model to a size of 100×50 km and proportionally increase the wavelength, and the model is interpolated to use the uniform grid. The settings of the source and receiver are the same as the homogeneous model mentioned previously. The meshing of the global domain is $400\,\Delta x \times 200\,\Delta z$, where $\Delta x = \Delta z = 250$ m, with five GLL points per direction; and the meshing of local domain is $400\,\Delta x \times 200\,\Delta z$, where $\Delta x = \Delta z = 50$ m, with three points per direction. It is of note that the grid size in the heterogeneous model is smaller than in the homogeneous model because it is

proportional to the slowest velocity, which is 1500 m/s in our Marmousi model. The time step of the global and local simulations is $\Delta t = 0.0025$ s.

The workflow for this experiment is the same as it was for the previous 2D homogeneous model. First, we perform a global simulation and calculate the hybrid inputs for the local simulations by using the Lagrange interpolation and the proposed MSI methods, respectively. Next, these two hybrid inputs are imposed on the hybrid interface to serve as the sources of the local simulation.

Figures 11A shows the wavefield of the global simulation at *t = 13s*, and Figures 11B and C show the associated wavefields of these two local simulations. Figure 12 displays the waveform comparison between the global and the local simulations in 2D Marmousi model. The total error of the Lagrange interpolation is E=0.09%, while the total error of the MSI method is E=0.02%. It is of note that the error waveforms are enlarged *10^3* times, implying that the overall error is lower than that of the 2D homogeneous model (Figure 7). This is because the accuracy of the numerical simulations depends on the amount of the grids per wavelength. The results of this experiment show that the proposed MSI method also has a salient effect in the heterogeneous medium.
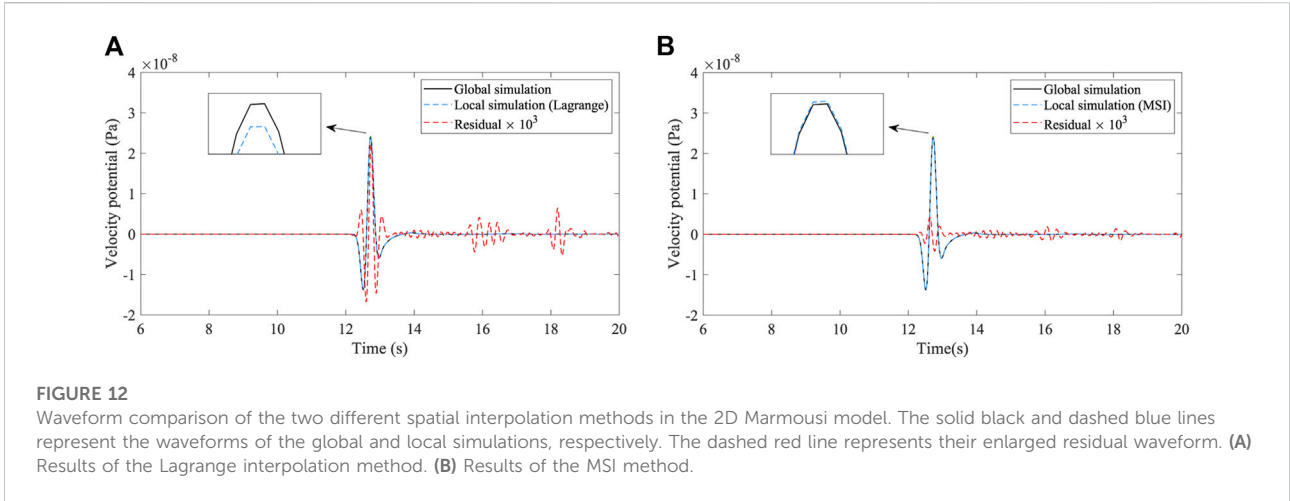
FIGURE 12
Waveform comparison of the two different spatial interpolation methods in the 2D Marmousi model. The solid black and dashed blue lines represent the waveforms of the global and local simulations, respectively. The dashed red line represents their enlarged residual waveform. **(A)** Results of the Lagrange interpolation method. **(B)** Results of the MSI method.
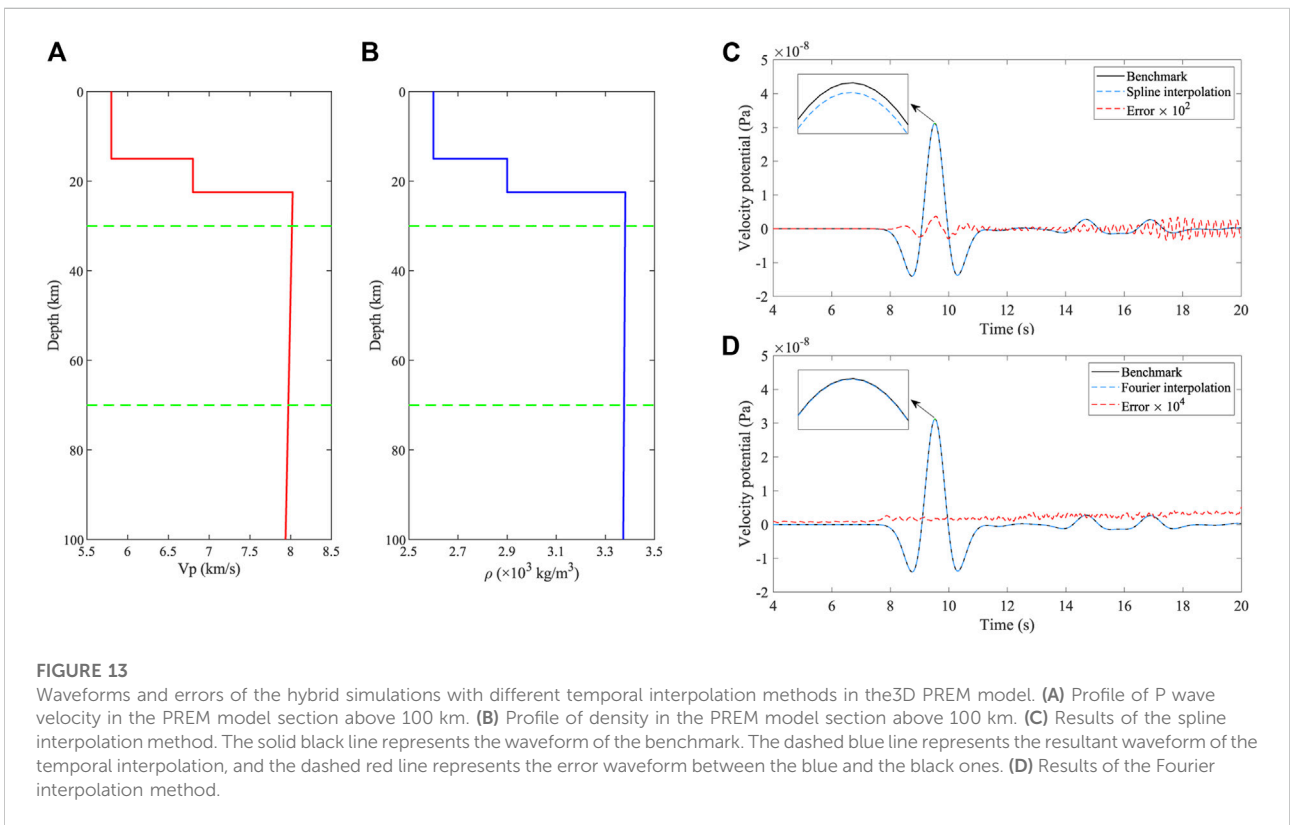

FIGURE 13
Waveforms and errors of the hybrid simulations with different temporal interpolation methods in the3D PREM model. **(A)** Profile of P wave velocity in the PREM model section above 100 km. **(B)** Profile of density in the PREM model section above 100 km. **(C)** Results of the spline interpolation method. The solid black line represents the waveform of the benchmark. The dashed blue line represents the resultant waveform of the temporal interpolation, and the dashed red line represents the error waveform between the blue and the black ones. **(D)** Results of the Fourier interpolation method.

3.3 3D hybrid numerical simulations in the PREM model

To verify the feasibility of the proposed methods, we consider a realistic 3D Earth model with the size of 200×200×100 km. The P wave velocity and density are stratified in z direction based on the PREM model section above 100 km (Figures 13A, B). In the PREM model, we removed the water layer and extended the crust layer to the surface. The local model, with the size of 50×50×40 km, is placed at the center of the global model. We set the dominant frequency of the Ricker wavelet to 0.5 Hz, which is close to the realistic frequency range in the lithosphere imaging of remote P waves. The source is in the center of the model surface, and the receiver is in the center of the entire model. To reduce the spatial dispersion in both the global and local simulations, the mesh is constructed according to the wave velocity of 3750 km/s, which is denser than the mesh according to the minimum wave velocity of 5,800 km/s in our PREM model.
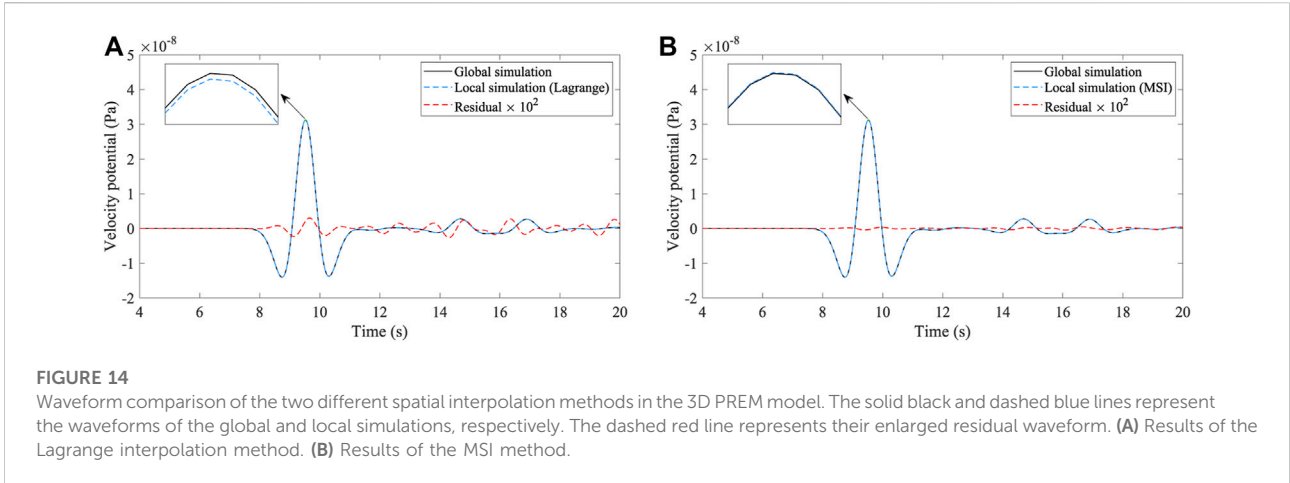
FIGURE 14
Waveform comparison of the two different spatial interpolation methods in the 3D PREM model. The solid black and dashed blue lines represent the waveforms of the global and local simulations, respectively. The dashed red line represents their enlarged residual waveform. **(A)** Results of the Lagrange interpolation method. **(B)** Results of the MSI method.

3.3.1 Validation and comparison of the Fourier interpolation method with a traditional method

Similar to the case in the 2D homogeneous model mentioned previously, we design an experiment with different temporal interpolation methods. We set the same grid size of $\Delta x = \Delta y = \Delta z = 2500$ m with five GLL points per direction in the global and local domains; thus, the global domain has $80 \times 80 \times 40$ elements and the local domain has $20 \times 20 \times 16$ elements. The time step of the global and local simulations is $\Delta t = 0.005$ s and the total duration is $4000\,\Delta t$. We take the simulation that the stored time interval of the hybrid inputs equates to the time step Δt of the simulations as the benchmark. Then, the stored time interval is enlarged to $40\,\Delta t$ and recovered to original time interval Δt by using traditional spline interpolation and proposed Fourier interpolation methods, respectively.

Figures 13C and D show the resultant waveforms of these two methods. It is of note that the error waveform of the spline interpolation is enlarged by 10^2 times, while the error waveform of the Fourier interpolation is enlarged by 10^4 times; thus, the error of the Fourier interpolation is reduced by about two orders of magnitude. This means that our method also works well in a 3D realistic model.

3.3.2 Validation and comparison of MSI with a traditional method

We adopt different meshing between the global and local domains to test the accuracy of the proposed spatial interpolation method in the 3D realistic model. The meshing of the global domain is $80\Delta x \times 80\,\Delta y \times 40\,\Delta z$, where $\Delta x = \Delta y = \Delta z = 2500$ m, with five GLL points per direction, and the meshing of the local domain is $40\,\Delta x \times 40\,\Delta y \times 32\,\Delta z$, where $\Delta x = \Delta y = \Delta z = 1250$ m, with five GLL points per direction. The time step of simulations is $\Delta t = 0.01$ s. We perform two hybrid simulations with the hybrid inputs are computed by using the traditional Lagrange interpolation and MSI methods, respectively.
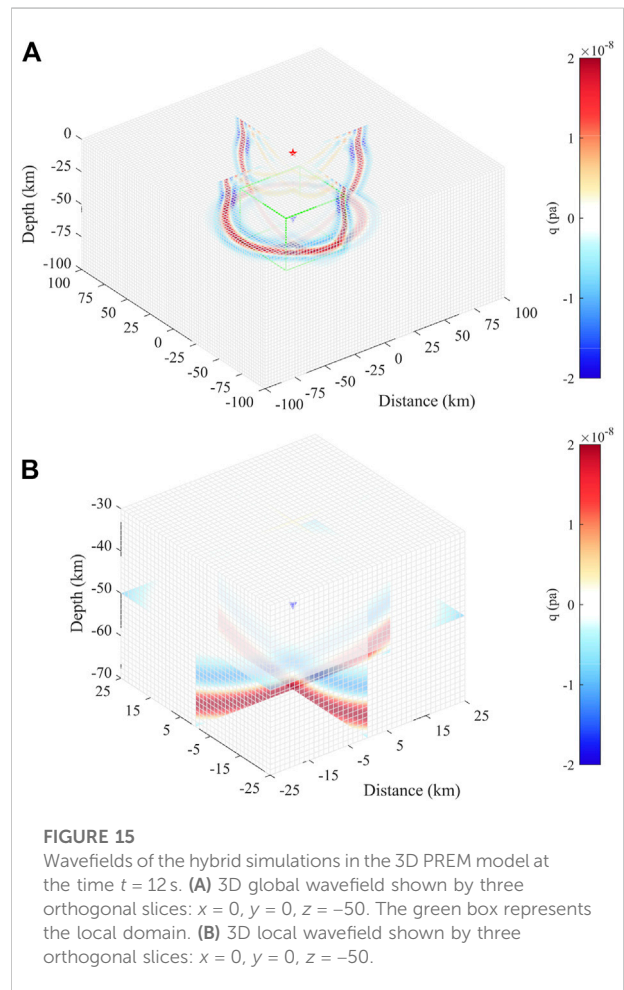

FIGURE 15
Wavefields of the hybrid simulations in the 3D PREM model at the time $t = 12$ s. **(A)** 3D global wavefield shown by three orthogonal slices: $x = 0$, $y = 0$, $z = -50$. The green box represents the local domain. **(B)** 3D local wavefield shown by three orthogonal slices: $x = 0$, $y = 0$, $z = -50$.

Figure 14 displays the results of the traditional Lagrange interpolation and the proposed MSI methods. The total error of the Lagrange interpolation is E=0.18%, while the total error of the MSI method is E=0.03%. Because we use denser

grid in the 3D model, the spatial dispersion in the 3D model is relatively small compared to the 2D cases. However, there are still large errors in the hybrid simulation, indicating that this error is primarily due to inaccurate hybrid inputs caused by spatial interpolation. The great improvement of waveform agreement validates the effectiveness of the MSI method in the 3D realistic model. Figures 15A and B show the wavefields of the global and local simulations at the time $t = 12$ s, respectively. It should be noted that we do not discern the hybrid wavefields calculated using Lagrange interpolation and MSI methods as they are almost the same in visual.

4 Discussion

4.1 Error of the hybrid simulation

In this article, we first introduced the Fourier interpolation into the hybrid simulation method, which outperforms the traditional spline interpolation method at high upsampling ratios (Figure 6). The requirement for the Fourier interpolation is that the data must be band-limited below the Nyquist limit (Zhang et al., 2017). This requirement can be readily fulfilled by introducing a smooth tapering window function. In our experiments, the accuracy of the Fourier interpolation method is improved by approximately three orders of magnitude than the traditional spline method in both 2D and 3D models (Figures 4 and 13). The statistical tests also show that the Fourier interpolation method is superior to the traditional Spline interpolation method below the Nyquist limit, especially at high upsampling ratios (Figure 6). Since the Fourier interpolation is theoretically exact, the extra errors may result from the window function altering the stored hybrid inputs. In addition, the distribution of the Fourier interpolation errors (Figures 4B and 13B) is similar to random noise.

When the meshing of the global and local domains is the same, the discrete differentiation method proposed by Masson et al. (2014) is an exact hybrid numerical simulation method (Figure 3). The hybrid simulation method, in fact, is related more closely to the scattering problem, that is, the small-scale perturbation in the local model concerning the global reference model. To better imagine the local small-scale structures, we must refine the local meshing with a smaller size. For the different meshing, there are errors between the global and local simulations introduced by the inaccurate hybrid inputs due to spatial interpolation.

In the spatial experiments, the errors of the hybrid simulation result from different spatial dispersions in the global and local simulations and inaccurate hybrid inputs. The spatial dispersion is an intrinsic and inevitable property of numerical simulations, but the accuracy of the hybrid inputs can be further improved by the proposed MSI method. In the 2D homogeneous model (Figure 7), the

total error of the MSI method (E=0.9%) is lower than the total error of the traditional Lagrange interpolation method (E=5.3%). In addition, we test the accuracy of the MSI method in the heterogeneous and 3D PREM models and obtain similar results (Figures 12 and 14) as in the 2D homogeneous model. This implies that our method has great potential to be applied in the realistic Earth model.

Though we use structural meshes in the simulations, the interpolation grid of the MSI method is uneven because it is built from GLL points rather than elements. Thus, this method can be naturally applied to non-structural meshes.

Importantly, in the case where the spatial and temporal errors are coupled, inaccurate spline interpolation in the time domain may further enlarge the spatial errors such that the Fourier interpolation method is necessary to minimize the errors of the hybrid simulation (Figures 9A and B). The prerequisite for both spline and Fourier interpolation methods is that the original hybrid inputs should be as accurate as possible. If the errors introduced by spatial-interpolation (Lagrange or MSI) methods are too large, there has no distinct discrepancy between the spline and Fourier interpolations in the time domain (Figures 9C and D). In other words, the spatial errors are dominant, and the temporal errors can be negligible.

Although the error of the hybrid simulation is discussed in this study, the proposed MSI method has potential applications in other fields. In many practical applications of SEM, the wavefields are not stored at all GLL points, but only the wavefields with a low sampling ratio are stored. Using the MSI method, the wavefield values at the existing GLL points can be used to construct more accurate global mean wavefields because the wavefield at each point has at least one element in each direction to constrain it. This has potential application value in the full waveform inversion. Because in the full waveform inversion, we do not need to record all the wavefields in the GLL points of unstructural meshes. Thus, based on the MSI method, we can construct an interpolation grid that encompasses the region to be interpolated and use the least squares method to invert the spline coefficients of the piecewise spline function in the entire interpolation grid. Then, we can repeatedly compute and store the wavefield at any position. In addition, for unstructural grid modeling, the MSI is also an effective local refinement scheme for interpolating wavefields from the coarse grid to the fine grid because the wavefield are always relatively smooth.

4.2 Numerical cost

The hybrid method is proposed to reduce the numerical cost by limiting the computation domain to a box region. In the forward simulation with SEM, the computational efficiency depends on the number of elements and time steps, and, thus,

the efficiency ratio between the global and local simulations is approximately expressed as follows:

$$\frac{T_1}{T_2} = \frac{nex_1 \times ney_1 \times nez_1 \times nt}{nex_2 \times ney_2 \times nez_2 \times nt}, \quad (26)$$

where nex, ney, and nez denote the number of elements in the x, y, and z directions, respectively. If the meshing of the global and local simulations is the same, the computational resources saved by hybrid method are proportional to the reduction of model dimension. For example, in our 3D temporal interpolation experiment (Section 3.3.1), the global domain has 80×80×40 elements and the local domain has 20×20×16 elements. The time step of the global and local domain is Δt=0.005s and the total duration is 4000Δt. In this configuration, the global simulation takes about 160.8 min (1 CPU), and the local simulation takes about 4 min (1 CPU), which is closed to 1/40 (20×20×16/80×80×40, according to Eq. (26)) as the global one due to the reduction of the model size. It is of note that the global simulation includes extra computation times for the calculation of hybrid inputs at much larger time step. Therefore, this is useful in situations where the source and receivers are located far away from the study region. It is of note that the dimension of the local targe model can be assigned arbitrarily, depending on the study region of interest.

According to Equations (9) and (10), to use the hybrid method, we must know the velocity potentials exactly on the GLL points within the hybrid elements, which are used to calculated the equivalent forces in the local simulation. For a 3D local targe model buried in the deep Earth with nex, ney, and nez elements with $N + 1$ GLL points per direction, the total number of stored values is

$$V = (nax_1 \times nay_1 \times naz_z - nax_2 \times nay_2 \times naz_2) \times nt \quad (27)$$

where $nax_1 = nex \times N + 1$, $nay_1 = ney \times N + 1$, $naz_1 = nez \times N + 1$; $nax_2 = (nex - 2) \times N - 1$, $nay_2 = (ney - 2) \times N - 1$, $naz_2 = (nez - 2) \times N - 1$. When the dimension of the local model is too large or the high-order SEM is used, the memory demand becomes exceedingly high. Owing to the great precision of the Fourier interpolation, we can store hybrid inputs with a large time interval on disk and significantly minimize the memory demand, especially in 3D cases. For example, in our 3D experiment, the grid used in the local simulation has a dimension of $20\Delta x \times 20\Delta y \times 16\Delta z$ with five GLL points per direction. The total duration of the simulation is $4000\Delta t$, where $\Delta t = 0.005$ s. In this configuration, if we store the hybrid inputs with the time interval equates to Δt, the number of stored wavefield values is 149,210×4,000, about 4.55 GB. When we increase the stored time interval to $40\Delta t$, the memory demand will be reduced by 40 times, about 113.8 MB.

Although the spatial MSI method will increase computational complexity as more elements are used to compute the hybrid inputs, the extra computational cost can be negligible compared with the process of globally solving wave propagation. We only need to calculate and save the hybrid inputs by the MSI spatial-interpolation at a very large time interval due to the preciseness of the introduction of Fourier temporal interpolation.

It is of note that this study did not include the case that receivers are located outside the local domain. In this case, the seismic response is handled through the wavefield extrapolation method (Masson and Romanowicz, 2017b), and the associated error propagation must be discussed. Another limitation of the study is that we only consider the error propagation of hybrid numerical simulation in the acoustic case using SEM. Considerably more work, such as the elastic wave, solid-fluid coupling cases, and other numerical methods, will need to be carried out in the future.

5 Conclusion

The aim of the present research was to control the error of the two-step hybrid method while the hybrid inputs are obtained by the direct discrete differentiation method. We find that the errors exist only when the meshing of the global and local simulations differs, and we propose a new spatial interpolation method, the multi-elements spline interpolation method, that outperforms the traditional Lagrange interpolation method. In addition, to save memory requirements, we introduce the Fourier interpolation method to the hybrid method, which allows us to store hybrid inputs with a large time interval. We also tested our methods in various models, and the results indicate that our methods not only improve the accuracy of the hybrid simulation but also significantly lower the memory demand, which has a high potential for application in probing the multi-scale structures of the Earth.

Data availability statement

The raw data supporting the conclusions of this article will be made available by the authors, without undue reservation.

Author contributions

HS, XT, CL, and LZ contributed to the conception of the study. HS performed the numerical simulations and wrote the first draft. CL and XT contributed significantly to analysis and manuscript preparation. LZ helped perform the analysis with constructive discussions.

Funding

41888101) and the China Scholarship Council (File no. 201804910289).

Conflict of interest

Publisher's note

References

Bielak, J., Loukakis, K., Hisada, Y., and Yoshimura, C. (2003). Domain reduction method for three-dimensional earthquake modeling in localized regions, Part I: Theory. *Bull. Seismol. Soc. Am.* 93 (2), 817–824. doi:10.1785/0120010251

Bozdağ, E., Peter, D., Lefebvre, M., Komatitsch, D., Tromp, J., Hill, J., et al. (2016). Global adjoint tomography: First-generation model. *Geophys. J. Int.* 207 (3), 1739–1766. doi:10.1093/gji/ggw356

Capdeville, Y., Chaljub, E., Vilotte, J. P., and Montagner, J. P. (2003). Coupling the spectral element method with a modal solution for elastic wave propagation in global Earth models. *Geophys. J. Int.* 152(1), 34–67. doi:10.1046/j.1365-246X.2003.01808.x

Capdeville, Y., and Métivier, L. (2018). Elastic full waveform inversion based on the homogenization method: Theoretical framework and 2-D numerical illustrations. *Geophys. J. Int.* 213 (2), 1093–1112. doi:10.1093/gji/ggy039

Chen, M., Niu, F., Liu, Q., and Tromp, J. (2015). Mantle-driven uplift of Hangai Dome: New seismic constraints from adjoint tomography. *Geophys. Res. Lett.* 42 (17), 6967–6974. doi:10.1002/2015gl065018

Chen, M., Niu, F., Tromp, J., Lenardic, A., Lee, C.-T. A., Cao, W., et al. (2017). Lithospheric foundering and underthrusting imaged beneath Tibet. *Nat. Commun.* 8 (1), 15659–15710. doi:10.1038/ncomms15659

Clouzet, P., Masson, Y., and Romanowicz, B. (2018). Box tomography: First application to the imaging of upper-mantle shear velocity and radial anisotropy structure beneath the North American continent. *Geophys. J. Int.* 213 (3), 1849–1875. doi:10.1093/gji/ggy078

Cox, M. G. (1972). The numerical evaluation of B-splines. *IMA J. Appl. Math.* 10 (2), 134–149. doi:10.1093/imamat/10.2.134

Fichtner, A. (2010). *Full seismic waveform modelling and inversion*. Springer Science & Business Media.

Frankel, A. (1993). Three-dimensional simulations of ground motions in the San Bernardino Valley, California, for hypothetical earthquakes on the San Andreas fault. *Bull. Seismol. Soc. Am.* 83 (4), 1020–1041. doi:10.1785/bssa0830041020

Fraser, D. (1989). Interpolation by the FFT revisited-an experimental investigation. *IEEE Trans. Acoust.* 37 (5), 665–675. doi:10.1109/29.17559

French, S., and Romanowicz, B. A. (2014). Whole-mantle radially anisotropic shear velocity structure from spectral-element waveform tomography. *Geophys. J. Int.* 199 (3), 1303–1327. doi:10.1093/gji/ggu334

French, S. W., and Romanowicz, B. (2015). Broad plumes rooted at the base of the Earth's mantle beneath major hotspots. *Nature* 525 (7567), 95–99. doi:10.1038/nature14876

Hayes, J. G., and Halliday, J. (1974). The least-squares fitting of cubic spline surfaces to general data sets. *Teach. Math. Appl.* 14 (1), 89–103. doi:10.1093/teamat/14.1.89

He, Y., Wen, L., Capdeville, Y., and Zhao, L. (2015). Seismic evidence for an Iceland thermo-chemical plume in the Earth's lowermost mantle. *Earth Planet. Sci. Lett.* 417, 19–27. doi:10.1016/j.epsl.2015.02.028

Igel, H. (2017). *Computational seismology: A practical introduction*. Oxford University Press.

Kelly, K. R., Ward, R. W., Treitel, S., and Alford, R. M. (1976). Synthetic seismograms: A finite-difference approach. *Geophysics* 41 (1), 2–27. doi:10.1190/1.1440605

Koene, E. F., Robertsson, J. O., Broggini, F., and Andersson, F. (2018). Eliminating time dispersion from seismic wave modeling. *Geophys. J. Int.* 213 (1), 169–180. doi:10.1093/gji/ggx563

Komatitsch, D., Barnes, C., and Tromp, J. (2000). Simulation of anisotropic wave propagation based upon a spectral element method. *Geophysics* 65 (4), 1251–1260. doi:10.1190/1.1444816

Komatitsch, D., and Tromp, J. (1999). Introduction to the spectral element method for three-dimensional seismic wave propagation. *Geophys. J. Int.* 139 (3), 806–822. doi:10.1046/j.1365-246x.1999.00967.x

Komatitsch, D., and Vilotte, J.-P. (1998). The spectral element method: An efficient tool to simulate the seismic response of 2D and 3D geological structures. *Bull. Seismol. Soc. Am.* 88 (2), 368–392.

Lei, W., Ruan, Y., Bozdağ, E., Peter, D., Lefebvre, M., Komatitsch, D., et al. (2020). Global adjoint tomography—Model GLAD-M25. *Geophys. J. Int.* 223 (1), 1–21. doi:10.1093/gji/ggaa253

Levander, A. R. (1988). Fourth-order finite-difference P-SV seismograms. *Geophysics* 53 (11), 1425–1436. doi:10.1190/1.1442422

Lin, C., Monteiller, V., Wang, K., Liu, T., Tong, P., and Liu, Q. (2019). High-frequency seismic wave modelling of the deep earth based on hybrid methods and spectral-element simulations: A conceptual study. *Geophys. J. Int.* 219 (3), 1948–1969. doi:10.1093/gji/ggz413

Lyu, C., Capdeville, Y., Al-Attar, D., and Zhao, L. (2021). Intrinsic non-uniqueness of the acoustic full waveform inverse problem. *Geophys. J. Int.* 226 (2), 795–802. doi:10.1093/gji/ggab134

Lyu, C., Capdeville, Y., and Zhao, L. (2020). Efficiency of the spectral element method with very high polynomial degree to solve the elastic wave equation. *Geophysics* 85 (1), T33–T43. doi:10.1190/geo2019-0087.1

Lyu, C., Zhao, L., and Capdeville, Y. (2022). Novel hybrid numerical simulation of the wave equation by combining physical and numerical representation theorems and a review of hybrid methodologies. *JGR. Solid Earth* 127, e2021JB022368. doi:10.1029/2021jb022368

Masson, Y., Cupillard, P., Capdeville, Y., and Romanowicz, B. (2014). On the numerical implementation of time-reversal mirrors for tomographic imaging. *Geophys. J. Int.* 196 (3), 1580–1599. doi:10.1093/gji/ggt459

Masson, Y., and Romanowicz, B. (2017a). Box tomography: Localized imaging of remote targets buried in an unknown medium, a step forward for understanding key structures in the deep earth. *Geophys. J. Int.* 211 (1), 141–163. doi:10.1093/gji/ggx141

Masson, Y., and Romanowicz, B. (2017b). Fast computation of synthetic seismograms within a medium containing remote localized perturbations: A numerical solution to the scattering problem. *Geophys. J. Int.* 208 (2), 674–692. doi:10.1093/gji/ggw412

Monteiller, V., Beller, S., Plazolles, B., and Chevrot, S. (2021). On the validity of the planar wave approximation to compute synthetic seismograms of teleseismic body waves in a 3-D regional model. *Geophys. J. Int.* 224 (3), 2060–2076. doi:10.1093/gji/ggaa570

Monteiller, V., Chevrot, S., Komatitsch, D., and Fuji, N. (2013). A hybrid method to compute short-period synthetic seismograms of teleseismic body waves in a 3-D regional model. *Geophys. J. Int.* 192 (1), 230–247. doi:10.1093/gji/ggs006

Monteiller, V., Chevrot, S., Komatitsch, D., and Wang, Y. (2015). Three-dimensional full waveform inversion of short-period teleseismic wavefields based upon the SEM–DSM hybrid method. *Geophys. J. Int.* 202 (2), 811–827. doi:10.1093/gji/ggv189

Oppenheim, A. V., Schafer, R. W., and Buck, J. R. (1999). *Discrete-Time Signal Processing*, 2nd Edition. New York: Prentice-Hall.

Replumaz, A., Kárason, H., van der Hilst, R. D., Besse, J., and Tapponnier, P. (2004). 4-D evolution of SE Asia's mantle from geological reconstructions and seismic tomography. *Earth Planet. Sci. Lett.* 221 (1-4), 103–115. doi:10.1016/s0012-821x(04)00070-6

Robertsson, J. O., Blanch, J. O., and Symes, W. W. (1994). Viscoelastic finite-difference modeling. *Geophysics* 59 (9), 1444–1456. doi:10.1190/1.1443701

Robertsson, J. O., and Chapman, C. H. (2000). An efficient method for calculating finite-difference seismograms after model alterations. *Geophysics* 65 (3), 907–918. doi:10.1190/1.1444787

Sacchi, M. D., Ulrych, T. J., and Walker, C. J. (1998). Interpolation and extrapolation using a high-resolution discrete Fourier transform. *IEEE Trans. Signal Process.* 46 (1), 31–38. doi:10.1109/78.651165

Schafer, R. W., and Rabiner, L. R. (1973). A digital signal processing approach to interpolation. *Proc. IEEE* 61 (6), 692–702. doi:10.1109/proc.1973.9150

Seriani, G., and Priolo, E. (1994). Spectral element method for acoustic wave simulation in heterogeneous media. *Finite Elem. analysis Des.* 16 (3-4), 337–348. doi:10.1016/0168-874x(94)90076-0

Tape, C., Liu, Q., Maggi, A., and Tromp, J. (2009). Adjoint tomography of the southern California crust. *Science* 325 (5943), 988–992. doi:10.1126/science.1175298

Tarantola, A. (1984). Inversion of seismic reflection data in the acoustic approximation. *Geophysics* 49 (8), 1259–1266. doi:10.1190/1.1441754

Tarantola, A. (1988). "Theoretical background for the inversion of seismic waveforms, including elasticity and attenuation," in *Scattering and attenuations of seismic waves, part i* (Springer), 365–399.

Tromp, J. (2020). Seismic wavefield imaging of Earth's interior across scales. *Nat. Rev. Earth Environ.* 1 (1), 40–53. doi:10.1038/s43017-019-0003-8

Tromp, J., Tape, C., and Liu, Q. (2005). Seismic tomography, adjoint methods, time reversal and banana-doughnut kernels. *Geophys. J. Int.* 160 (1), 195–216. doi:10.1111/j.1365-246x.2004.02453.x

Van Der Meer, D. G., Zeebe, R. E., van Hinsbergen, D. J., Sluijs, A., Spakman, W., and Torsvik, T. H. (2014). Plate tectonic controls on atmospheric CO2 levels since the Triassic. *Proc. Natl. Acad. Sci. U. S. A.* 111 (12), 4380–4385. doi:10.1073/pnas.1315657111

Virieux, J., and Operto, S. (2009). An overview of full-waveform inversion in exploration geophysics. *Geophysics* 74 (6), WCC1–WCC26. doi:10.1190/1.3238367

Wang, Y., Chevrot, S., Monteiller, V., Komatitsch, D., Mouthereau, F., Manatschal, G., et al. (2016). The deep roots of the Western Pyrenees revealed by full waveform inversion of teleseismic P waves. *Geology* 44 (6), 475–478. doi:10.1130/g37812.1

Wen, L. (2002). An SH hybrid method and shear velocity structures in the lowermost mantle beneath the central Pacific and South Atlantic Oceans. *J. Geophys. Res.* 107 (B3), 2055–2120. doi:10.1029/2001jb000499

Wen, L., and Helmberger, D. V. (1998). A two dimensional P SV hybrid method and its application to modeling localized structures near the core mantle boundary. *J. Geophys. Res.* 103 (B8), 17901–17918. doi:10.1029/98jb01276

Yoshimura, C., Bielak, J., Hisada, Y., and Fernández, A. (2003). Domain reduction method for three-dimensional earthquake modeling in localized regions, part II: Verification and applications. *Bull. Seismol. Soc. Am.* 93 (2), 825–841. doi:10.1785/0120010252

Zhang, J., Yao, Z. J. E., and Physics, P. (2017). Exact local refinement using Fourier interpolation for nonuniform-grid modeling. *Earth Planet. Phys.* 1 (1), 58–62. doi:10.26464/epp2017008

Zhang, L., and Zhang, J. (2022). Local wavefield refinement using Fourier interpolation and boundary extrapolation for finite-element method based on domain reduction method. *Geophysics* 87 (3), T251–T263. doi:10.1190/geo2021-0503.1

Zhao, L., Allen, R. M., Zheng, T., and Zhu, R. (2012). High-resolution body wave tomography models of the upper mantle beneath eastern China and the adjacent areas. *Geochem. Geophys. Geosyst.* 13 (6). doi:10.1029/2012gc004119

Zhao, L., Wen, L., Chen, L., and Zheng, T. (2008). A two-dimensional hybrid method for modeling seismic wave propagation in anisotropic media. *J. Geophys. Res.* 113 (B12), B12307. doi:10.1029/2008jb005733

Zhao, M., Capdeville, Y., and Zhang, H. (2016). Direct numerical modeling of time-reversal acoustic subwavelength focusing. *Wave Motion* 67, 102–115. doi:10.1016/j.wavemoti.2016.07.010

Zhu, H., Bozdağ, E., Peter, D., and Tromp, J. (2012). Structure of the European upper mantle revealed by adjoint tomography. *Nat. Geosci.* 5 (7), 493–498. doi:10.1038/ngeo1501